1

Th/U ratios in metamorphic zircon

2

3

Chris Yakymchuk[1],*, Christopher L. Kirkland[2], Chris Clark[2]

4

5   [1]Department of Earth and Environmental Sciences, University of Waterloo, Waterloo, Ontario, Canada,

6   N2L 3G1, *cyakymchuk@uwaterloo.ca

7

8   [2]Department of Applied Geology, Curtin University, Perth, Western Australia, Australia, 6102

9   **ABSTRACT**

10   The Th/U ratios of zircon crystals are routinely used to help understand their growth mechanism.

11   Despite the wide application of Th/U ratios in understanding the geological significance of zircon U–Pb

12   ages, the main controls on the Th/U ratio in metamorphic zircon are poorly understood. Here, phase

13   equilibria modelling coupled with solubility expressions for accessory minerals are used to investigate

14   the controls on the Th/U ratios of suprasolidus metamorphic zircon in an average amphibolite-facies

15   metapelite composition. We also present a new database of metamorphic Th/U ratios in zircon from

16   Western Australia. Several factors affecting the Th/U ratio are investigated, including the bulk rock

17   concentrations of Th and U, the amount of monazite and apatite in the system, and open versus closed

18   system behaviour. Our modelling predicts that the main controls on the Th/U ratio of suprasolidus

19   metamorphic zircon are the concentrations of Th and U in the system and the breakdown and growth of

20   monazite in equilibrium with zircon. Furthermore, the relative timing of zircon and monazite growth

21   during cooling and melt crystallization has an important role in the Th/U ratio of zircon. Early grown

22   zircon near the peak of metamorphism is expected to have elevated Th/U ratios whereas zircon that grew

23   near the solidus is predicted to have relatively low Th/U ratios, which reflects the coeval growth of

24   monazite during cooling and melt crystallization. Our modelling approach aims to provide an improved

25   understanding of the main controls of Th/U in metamorphic zircon in migmatites and hence better apply

26   this geochemical ratio as a tool to assist in interpretation of the genesis of metamorphic zircon.

27

28   **KEY WORDS**: zircon, Th/U, monazite, metamorphic, migmatite, phase equilibria

29

30   **1 INTRODUCTION**

31   Zircon U–Pb geochronology is a powerful tool in determining the absolute timing, duration and hence

32   geodynamic significance of metamorphic events (Harley, Kelly, & Möller, 2007; Rubatto & Hermann,

33   2007; Rubatto, 2017). In igneous rocks, magmatic zircon grows during the crystallization of melt when

34   the melt reaches saturation in Zr with respect to zircon (e.g. Boehnke, Watson, Trail, Harrison, &

35   Schmitt, 2013). In metamorphic systems, zircon can grow or recrystallize at P–T conditions below the

36   solidus (subsolidus metamorphic zircon) or crystallize from melt above the solidus (suprasolidus

37   metamorphic zircon or anatectic zircon).

38   Zircon in igneous and metamorphic systems concentrates U and Th, which permits

39   geochronological investigation and the concentration of these elements in zircon has potential to help

40   elucidate the crystal's growth mechanism. Metamorphic rocks commonly contain multiple age

41   populations of zircon that reflect both inherited and newly grown material, with the Th/U ratio used as a

42   tool to distinguish between different populations (Hoskin & Schaltegger, 2003; Rubatto & Gebauer,

43   2000; Rubatto, 2002; Rubatto, 2017; Schaltegger et al., 1999; Williams & Claesson, 1987). A common

44   observation is that most metamorphic zircon has Th/U ratios <0.1, except in high-temperature and

45   ultrahigh-temperature (UHT) metamorphic rocks, where this ratio is frequently >0.1 (e.g. Harley et al.,

46   2007; Kelley & Harley, 2005; Kelsey & Hand, 2015; Korhonen, Clark, Brown, Bhattacharya, & Taylor,

47   2013; Rubatto, 2017; Vavra, Schmid, & Gebauer, 1996). However, the reasons for this variation in

48   zircon Th/U are not always clear.

49   An important control on the Th/U of zircon in metamorphic rocks may be the coeval growth of

50   Th-rich accessory minerals, such as monazite and allanite (Harley et al., 2007; Kelsey & Hand, 2015;

51   Kirkland, Smithies, Taylor, Evans, & McDonald, 2015; Schaltegger & Davies, 2017; Rubatto, 2017).

52   Monazite and allanite are expected to be the dominant hosts of Th in metamorphic rocks whereas zircon,

53   monazite, xenotime, apatite and allanite can share the majority of the U budget (Bea, 1996; Bea &

54   Montero, 1999; Hermann, 2002). The major rock-forming minerals contain a relatively minor proportion

3

55   of the Th and U in most metamorphic rocks. Therefore, the breakdown and growth of Th-rich (and to a

56   lesser extent U-rich) accessory minerals will have a major effect on the Th/U ratios of equilibrated

57   zircon.

58   Allanite is generally restricted to relatively high-Ca bulk compositions (Finger, Krenn, Schulz,

59   Harlov, & Schiller, 2016; Wing, Ferry, & Harrison, 2003) and subsolidus conditions in metapelites

60   (Spear & Pyle, 2010) whereas monazite is common in metapelites at subsolidus and suprasolidus

61   conditions. Above the solidus, monazite is the dominant reservoir of Th (e.g. Bea & Montero, 1999) due

62   to the large monazite–melt partition coefficient of Th relative to other minerals (e.g. Stepanov,

63   Hermann, Rubatto, & Rapp, 2012). During high-temperature metamorphism and anatexis, monazite is

64   expected to break down and hence saturate the anatectic melt in Light Rare Earth Elements (LREE). The

65   suprasolidus behaviour of monazite is a function of temperature, pressure, melt chemistry, bulk

66   composition (Duc-Tin & Keppler, 2015; Montel, 1986; Rapp & Watson, 1986; Rapp, Ryerson, &

67   Miller, 1987; Skora & Blundy, 2012; Stepanov et al., 2012). The growth and breakdown of apatite also

68   impacts the stability of monazite during anatexis (Johnson, Clark, Taylor, Santosh, & Collins, 2015;

69   Yakymchuk, 2017).

70   When monazite is present in an equilibrated system it is expected to host a large proportion of

71   the Th budget in the rock. Zircon in equilibrium with this monazite is expected to have relatively low

72   Th/U ratios (e.g. Cesare, Gómez-Pugnaire, & Rubatto, 2003; Rubatto, Williams, & Buick, 2001;

73   Rubatto, 2017; Vavra et al., 1996). If monazite becomes completely consumed during anatexis, zircon in

74   equilibrium with the melt could be expected to have relatively high Th/U ratios unless there is an

75   additional sink for Th. Therefore, in aluminous metasedimentary migmatites, one of the primary controls

76   on the Th/U ratio of equilibrated zircon is thought to be the presence or absence of monazite. However,

77   to our knowledge, no attempt has been made to quantitatively model the Th/U ratio of suprasolidus

78   metamorphic zircon in monazite-buffered systems and to evaluate other possible reasons for the

79   observed Th/U ratios in suprasolidus metamorphic zircon.

80   In this contribution, to provide context to our study we first present a database of Th/U ratios in

81   metamorphic and igneous zircon from Western Australia to evaluate the range of values in metamorphic

82   versus igneous zircon and show that a single threshold Th/U ratio is not always appropriate for

83   distinguishing the origin of zircon. To evaluate why metamorphic zircon can record a spread in Th/U

84   ratios, we then use forward phase equilibria modelling coupled with solubility equations for monazite,

85   apatite and zircon in anatectic melt to investigate the controls on Th/U ratios of metamorphic zircon in a

86   suprasolidus metapelite. We investigate several factors that can control Th/U ratios in suprasolidus

87   metamorphic zircon grains, including bulk-rock compositions, variations in partition coefficients, and

88   open-system behaviour. The modelling results presented here are generally applicable to suprasolidus

89   metamorphism of metasedimentary rocks that contain an equilibrium assemblage with accessory

90   monazite, zircon and apatite. Our findings have implications for interpreting Th/U ratios of zircon in

91   high-temperature and UHT metamorphic rocks.

92

93   **2 COMPILATION OF TH/U RATIOS IN METAMORPHIC ZIRCON**

94   The range of Th/U ratios in metamorphic zircon can vary over several orders of magnitude (e.g. Harley

95   et al., 2007; Hoskin & Schaltegger, 2003; Rubatto, 2017). To demonstrate the variability of Th/U ratios

96   in natural samples and the difference between igneous and metamorphic zircon, a SIMS dataset of 1352

97   analyses of metamorphic zircon and 5794 analyses of igneous zircon from published geochronology

98   results in Western Australia is summarized in Figure 1. The dataset for the metamorphic zircon group is

99   presented in supplementary Table S1. Data for the igneous group are from the compilation in Kirkland

100   et al. (2015). The data exclude analyses that have >10% U–Pb discordance in order to exclude metamict

101   zircon. Analyses have been categorised based on all or some of the following: cathodoluminescence

102   texture, isotopic date in relation to regional age patterns, lithology (e.g. metamorphosed versus

103   unmetamorphosed), and information from other isotopic systems including oxygen and $^{176}Hf/^{177}Hf$. All

104   such interpretations of zircon growth (e.g. igneous or metamorphic) are published in the Geological

105   Survey of Western Australia geochronology record series (http://www.dmp.wa.gov.au/geochron). For

106   the metamorphic zircon group, data include Archean, Proterozoic and Phanerozoic examples from the

107   major metamorphic belts in Western Australia, including the Pilbara, Yilgarn, Albany–Fraser Orogen,

108   Musgrave Province, Capricorn Orogen, Rudall Province as well as associated basins. The data record a

109   wide variety of metamorphic conditions and suprasolidus and subsolidus metamorphic zircon are not

110   distinguished.

111   The Th/U ratios of metamorphic zircon from Western Australia range from <0.001 to >10

112   (Figure 1a–d) and are highly skewed towards lower values (Figure 1a). The entire dataset yields a

113   median value of 0.44 and values of 0.08 and 1.08 for the 25th and 75th percentiles, respectively. The

114   distribution of the dataset is roughly log-normal (inset in Figure 1a), but the log-normalized dataset is

115   also slightly skewed towards lower ratios of Th/U ratios in zircon.

116   Thorium and U concentrations in metamorphic zircon are highly skewed towards low values

117   (Figure 1b, c). Concentrations of Th in zircon have a median value of 105 ppm and 25th and 75th

118   percentile values of 28 ppm and 232 ppm, respectively. The log-normalized Th concentration data is

119   also skewed towards low values (Figure 1b). Uranium concentrations in zircon have a median value of

120   252 ppm and 25th and 75th percentile values of 98 ppm and 616 ppm, respectively. Log-normalized U

121   concentrations are approximately normally distributed (Figure 1c).

122   The Th/U ratios of igneous zircon range from <0.01 to 20 (Figure 1d) with a median value of

123   0.68 and 25th and 75th percentile values of 0.49 and 0.98, respectively. The distribution of Th/U ratios in

124   igneous zircon is more symmetrical around the median than data for metamorphic zircon. Thorium

125   concentrations of igneous zircon have a median value of 125 ppm and 25th and 75th percentile values of

126   73 ppm and 222 ppm, respectively (Figure 1e). Unlike the distribution for metamorphic zircon (Figure

127   1b), Th concentrations in igneous zircon are not highly skewed towards low values (Figure 1b, e).

128   Uranium concentrations of igneous zircon have a median value of 186 ppm and 25th and 75th percentile

6

129   values of 110 ppm and 332 ppm, respectively (Figure 1f). The distributions of U concentrations in

130   metamorphic and igneous zircon are similar (Figure 1c, f).

131

132   **3 METHODOLOGY**

133   **3.1 Closed system**

134   Forward phase equilibria modelling of an average amphibolite-facies metapelite composition from Ague

135   (1991) is used to determine the proportions and major element compositions of major minerals and melt

136   from the wet solidus (~670°C) up to 950°C, at pressures from 0.5 to 1.2 GPa. Values were calculated in

137   a grid with intervals of 1°C and 0.01 GPa. Additionally, we model two isobaric heating paths at 0.6 and

138   0.9 GPa and one open-system scenario involving melt loss and isobaric heating at 0.9 GPa from the wet

139   solidus up to 950°C.

140   Calculations were conducted with THERMOCALC v.3.40 (Powell & Holland, 1988) and with the

141   internally consistent dataset (ds62) of Holland and Powell (2011). Modelling was undertaken in the

142      $MnO–Na_2O–CaO–K_2O–FeO–MgO–Al_2O_3–SiO_2–H_2O–TiO_2–Fe_2O_3$ (MnNCKFMASHTO) chemical

143   system with the activity–composition models of White, Powell, Holland, Johnson, and Green (2014).

144   The amount of H_2O in the bulk composition was adjusted so that the system was just saturated with H_2O

145   at the wet solidus at 0.9 GPa. For the 0.6 GPa isobaric heating path, the amount of H_2O was adjusted so

146   that the system was just saturated with H_2O at the wet solidus at 0.6 GPa. Modelled bulk compositions

147   are summarized in Table 1. Phases modelled as pure end-members include quartz, rutile, aqueous fluid

148   (H_2O), kyanite and sillimanite. To calculate the Th/U ratio in equilibrated metamorphic zircon, our

149   modelling approach requires: (1) proportions of the major and accessory minerals and melt at each $P–T$

150   condition, (2) partition coefficients of Th and U between melt and the major and accessory minerals at

151   each $P–T$ condition, (3) concentrations of Zr, LREE, P_2O_5, Th and U in the system.

152   Accessory mineral behaviour is calculated following the methodology of Kelsey et al. (2008) and are

153   discussed in detail elsewhere (Kelsey, Clark, & Hand, 2008; Yakymchuk & Brown, 2014b; Yakymchuk,

154 2017; Yakymchuk, Clark, & White, 2017). Briefly, melt compositions extracted from THERMOCALC are

155 combined with the solubility expressions for zircon (Boehnke et al., 2013), monazite (Stepanov et al.,

156 2012) and apatite (Wolf & London, 1994) to determine the saturation concentrations of Zr, LREE and

157 P_2O_5 at various P–T conditions. Because melt compositions across the phase diagram are peraluminous

158 with ASI (molar Al_2O_3/[$Na_2O + K_2O + CaO$]) values greater than 1.1—with the exception of the high-P

159 and low-T portion of the diagram (c.f. Yakymchuk, 2017)—we use the apatite solubility expression of

160 Wolf and London (1994) instead of other published expressions that were calibrated for metaluminous

161 and peralkaline melt compositions (e.g. Harrison & Watson, 1984). For the high-P and low-T portion of

162 the diagram, modelled melt composition have ASI values less than 1.1 and the solubility expression of

163 Wolf and London (1994) is not valid. Therefore, we assume that apatite is unreactive at these P–T

164 conditions.

165   Assumed bulk rock compositions of Zr, LREE and P are then combined with the solubility

166 expressions for zircon, monazite, and apatite along with stoichiometric concentrations of these elements

167 in accessory minerals and the proportion of melt in the system (estimated from THERMOCALC) to

168 determine the amount of accessory mineral dissolution necessary to saturate the anatectic melt in these

169 elements. We use stoichiometric values of Zr in zircon (497,664 ppm; Kelsey et al., 2008) and P_2O_5 in

170 apatite (41 wt.%; the average of apatite compositions reported in Webster & Piccoli, 2015). For

171 monazite, we start with a stoichiometric concentration of 566,794 ppm LREE (Kelsey et al., 2008) at the

172 solidus, but this is adjusted based on the calculated amount of Th in monazite above the solidus.

173 Throughout, we assume that the atomic weight of the LREE in monazite is 140 g/mol.

174   Weight fractions of accessory minerals at the solidus are determined from the bulk rock

175 concentrations and stoichiometric values of Zr, P and LREE. At the solidus, all Zr is assumed to reside

176 in zircon, all LREE is in monazite, and any P not allocated to form stoichiometric monazite ($LREEPO_4$)

177 resides in apatite. The concentration of LREE in apatite is determined by partitioning with anatectic melt

178 and a $D_{ap/melt}^{LREE}$ value of 10 is used (e.g. Prowatke & Klemme, 2006). Apatite is assumed to have no

8

179   LREE at the solidus. Above the solidus, the amount of LREE in apatite is subtracted from the bulk rock

180   composition and the remainder is used to calculate the mode of monazite and this process is done

181   iteratively to determine the amount of LREE and P allocated to form monazite and apatite (e.g.

182   Yakymchuk, 2017). No adjustment was made to the Ca concentration of the modelled metapelite

183   composition to account for apatite.

184   Monazite solubility is a function of temperature, pressure, melt composition and the Th

185   concentration of monazite (Stepanov et al., 2012). The concentration of Th in monazite is determined by

186   partitioning with melt. Partitioning of Th into monazite also decreases the saturation concentration of

187   LREE of the melt in monazite-bearing systems (e.g. Stepanov et al., 2012). The concentration of Th in

188   monazite and the concentration of LREE in monazite-saturated melt are calculated iteratively at each P–

189   T condition (e.g. Yakymchuk, 2017). At very low monazite modes at temperatures just below monazite

190   exhaustion, the modelling here predicts unrealistically high concentrations of ThO_2 (>30 wt.%) in

191   monazite. Therefore, we set a minimum X_{LREE} value of 0.7, where X_{LREE} represents the molar ratio of the

192   LREE to other cations (Th in the modelling here) in monazite (Stepanov et al., 2012). Thorium and U

193   are treated as trace elements and not as essential structural constituents (e.g. Sun & Hanson, 1975) of the

194   accessory minerals. Therefore, their concentrations in anatectic melt are determined by partition

195   coefficients between these elements and the modes of the major and accessory minerals. At each

196   modelled P–T point, the proportions of the major minerals and melt (calculated by THERMOCALC) and

197   the weight fraction of the accessory minerals are coupled with mineral/melt partition coefficients of Th

198   and U and the concentrations of Th and U in the system (e.g. bulk rock compositions) to determine the

199   concentrations of Th and U in the melt using a batch melting model (e.g. Shaw, 1970; Hanson, 1978).

200   Concentrations of Th and U in minerals are determined from the mineral/melt partition coefficients and

201   the calculated concentrations of Th and U in melt. The proportions of Th and U in the system hosted by

202   the different phases are calculated by combining phase proportions with the calculated concentrations of

203   Th and U in each phase.

9

204   Partition coefficients for Th and U used in the modelling for the major minerals and apatite as well

205   as U for monazite are listed in Table 2. Partition coefficients for Th and U between zircon and anatectic

206   melt are a function of temperature and we use the partitioning expressions of Kirkland et al. (2015) to

207   model the Th and U concentrations and Th/U ratios of zircon that is in equilibrium with anatectic melt.

208   For U partitioning between monazite and melt, we use a value of 83, which is an average of the values

209   reported in Stepanov et al. (2012).

210   For monazite, partition coefficients of Th are highly variable between studies of natural samples and

211   experiments. Figure 2 is a compilation of Th concentrations of coexisting (assumed equilibrated)

212   monazite and melt from experiments and studies of volcanic rocks, S-type granites, nanogranites and

213   leucosomes in migmatites. Glasses from experimental studies have Th concentrations mostly ranging

214   from 100 to 1,000 ppm (Hermann & Rubatto, 2009; Skora & Blundy, 2010; Stepanov et al., 2012; Xing,

215   Trail, & Watson, 2013) with most estimated monazite–melt partition coefficients between 100 and 1,000

216   (Figure 2). The measured experimental glass compositions have roughly an order of magnitude more Th

217   than the range of Th concentrations measured in S-type granites (Ayers & Harris, 1997; Inger & Harris,

218   1993; Sawka & Chappel, 1986; Tartèse & Boulvais, 2010; Villaros, Stevens, Moyen, & Buick, 2009)

219   and leucosomes in metasedimentary migmatites (Korhonen, Saito, Brown, Siddoway, & Day, 2010;

220   Sawyer, 1987; Solar & Brown, 2001). For natural samples, Th concentrations of coexisting (assumed

221   equilibrated) monazite and melt (e.g. granite or leucosome) yield partition coefficients that mostly range

222   from 1,000 to 10,000 (Bea, Pereira, & Stroh, 1994; Breiter, 2016; Förster, 1998; Montel, 1993;

223   Pichavant et al., 1987; Wark & Miller, 1993; Weber, Barbey, Cuney, & Martin, 1985). Acosta-Vigil et

224   al. (2010) reported Th concentrations from monazite associated with nanogranites with a monazite–melt

225   partition coefficient of ~12,000. The Th concentration of volcanic Macusani glass (composition JV2

226   from Pichavant et al., 1987) paired with the average concentration of Th in monazite from Montel

227   (1993) yields a partition coefficient of ~38,000. Considering the wide range of reported and calculated

228   partition coefficients, we investigate different partition values but use a value for $D^{Th}_{mnz/melt}$ of 5,000 as

229   a baseline, which represents the high-end of values from experimental studies and an approximate

230   median for natural rocks.

231   Bulk compositions of Zr, LREE and P_2O_5 have important implications for the stability of zircon,

232   monazite and apatite during anatexis (Kelsey et al., 2008; Kelsey & Powell, 2011; Yakymchuk &

233   Brown, 2014b; Yakymchuk, 2017; Yakymchuk et al., 2017). Our modelled baseline scenario uses LREE

234   and Zr whole-rock concentrations of 150 ppm, which is a rough average of concentrations in fine-

235   grained sedimentary rocks and metasedimentary migmatites (Taylor & McLennan, 1985; Yakymchuk &

236   Brown, 2014) and a P_2O_5 concentration of 0.19 wt.%, which is an average of amphibolite-facies

237   metapelites reported in Ague (1991).

238   We investigate various bulk-rock concentrations of Th and U as well as Th/U ratios. Fine-grained

239   sedimentary rocks have Th/U ratios generally between 3.5 and 5.5 (Taylor & McLennan, 1985).

240   Thorium concentrations mostly range from 5 to 17 ppm and U concentrations vary from 1.5 to 4.0 ppm

241   (Taylor & McLennan, 1985). We use bulk concentrations of 3.5 ppm U and 14 ppm Th (average of <2.0

242   Ga fine-grained sedimentary rocks) in our baseline scenario.

243

244   **3.2 Open system**

245   Most migmatites and granulites yield field, petrographic and geochemical evidence for melt loss. The

246   preservation of high-temperature mineral assemblages in metamorphic rocks is consistent with the loss

247   of anatectic melt (e.g. Diener, White, & Powell, 2008; White & Powell, 2002). The geochemistry of

248   many granulites is also consistent with the loss of melt enriched in relatively incompatible elements (e.g.

249   Brown, 2013; Guernina & Sawyer, 2003). The extraction of melt from the anatectic crust has important

250   implications for the stability of accessory minerals (Kelsey et al., 2008; Yakymchuk & Brown, 2014b)

251   and the concentrations of the essential structural constituents of accessory minerals in the residuum (e.g.

252   Rapp et al., 1987). Because open-system behaviour in migmatites is path dependent (e.g. Guevara &

253   Caddick, 2016; Mayne, Moyen, Stevens, & Kaisl Aniemi, 2016) and each rock and $P–T$ path must be

11

254   evaluated on a case-by-case basis, we choose to model a simple isobaric heating path at 0.9 GPa from

255   the solidus up to a peak temperature of 950°C and use this to investigate the role of melt loss on the

256   Th/U ratio of suprasolidus metamorphic zircon.

257   Melt loss is modelled assuming that the system becomes open to melt extraction when the

258   proportion of melt reaches a critical threshold. We choose the 7 vol.% melt connectivity threshold of

259   Rosenberg and Handy (2005), which is a rheological threshold where melt along grain boundaries may

260   become interconnected throughout the rock framework. For the modelling, six-sevenths of the melt are

261   extracted leaving 1 vol.% in the system (e.g. Yakymchuk & Brown, 2014a). This amount of residual

262   melt is consistent with observations of thin films on grain boundaries in migmatites that are interpreted

263   to represent melt pseudomorphs (e.g. Holness & Sawyer, 2008), which suggests that migmatites retain a

264   portion of the melt. The major element chemistry of the melt is calculated by THERMOCALC and the trace

265   element concentrations are calculated from the saturation equations of monazite, zircon and apatite for

266   LREE, Zr and P. Concentrations of Th and U in the melt are calculated by partitioning. After each melt

267   loss event, the new melt-depleted composition is used to model the phase equilibria, accessory mineral

268   modes and Th/U values of zircon for the next segment of the isobaric heating path up to the next melt

269   loss event and so on.

270

271   **4 RESULTS**

272   The results for the baseline scenario for a closed system are plotted on a *P–T* diagram, which has been

273   contoured using Matlab$^{®}$. A smoothing filter based on a 3x3 Pascal triangle was applied to the results to

274   generate the plot, which minimizes the influence of very small fields on the contours across the diagram.

275   In addition, closed-system results for two isobaric heating paths (0.6 and 0.9 GPa) and one open-system

276   scenario (0.9 GPa isobaric heating) are presented, but no smoothing filter was applied to these results.

277

278   **4.1 P–T phase diagram**

279   The *P–T* phase diagram (pseudosection) for the average amphibolite-facies metapelite is shown in

280   Figure 3. The temperature of the solidus ranges from 670°C at 0.5 GPa to ~710°C at 1.2 GPa. Rutile is

281   restricted to relatively high pressures (>1.0 GPa). Ilmenite and plagioclase are stable across the entire

282   modelled *P–T* range. No orthopyroxene is predicted to be stable. A narrow field that represents

283   muscovite breakdown to K-feldspar extends from <680°C at 0.5 GPa to <790°C at 1.2 GPa. Biotite

284   breakdown melting occurs after muscovite exhaustion. At > 0.7 GPa, biotite breaks down to garnet over

285   100–150°C and biotite is completely consumed by ~850°C. A narrow high-variance field extending

286   from 770°C at 0.5 GPa to 850°C at 0.7 GPa represents the breakdown of biotite to cordierite. After

287   biotite exhaustion, melting proceeds via the consumption of quartz and feldspar. This sequence of

288   melting reactions with increasing temperature is common for most aluminous metasedimentary rocks

289   (e.g. Brown, 2013; Clemens, 2006). The modelled amount of melt in normalized molar percentage

290   (approximately equivalent to vol.%) is shown in Figure 4a. Melt proportion contours have steep positive

291   slopes, which indicates that more melt is generated at lower pressures and that melting can proceed via

292   heating and decompression, assuming closed-system behaviour. The amount of melt produced during

293   open system melting during heating and decompression is significantly less (e.g. Mayne et al., 2016;

294   Yakymchuk & Brown, 2014a).

295

296   **4.2 Accessory mineral proportions**

297   The amounts of zircon, monazite and apatite dissolution in the system relative to the amount of these

298   minerals at the solidus for the baseline scenario are illustrated in Figure 4b–d. The modelled proportions

299   for each accessory mineral are non-linear up temperature with closer spacing of contours at high-

300   temperature. Zircon and monazite dissolution contours are nearly vertical except in the narrow

301   muscovite–K-feldspar field at low temperatures and the narrow biotite–cordierite field at low pressures

302   and high temperatures where contours are less steeply sloping. Apatite proportions are strongly

303   controlled by the aluminum saturation index (ASI) of the melt (e.g. Wolf & London, 1994) and have

304 positive slopes except at low pressure and high temperature, where they are negatively sloping at P–T

305 conditions outside the stability field of sillimanite and biotite (Figure 3).

306

307 **4.3 Th/U in melt and zircon**

308 Concentrations of Th and U as well as the Th/U ratios of melt and zircon across the range of modelled

309 P–T conditions for the baseline scenario are shown in Figure 5. Concentrations of Th in melt increase up

310 temperature until monazite is exhausted (Figure 5a). The contours are closer spaced at higher T,

311 corresponding to an increased rate of dissolution at higher T. After monazite exhaustion, Th

312 concentrations decrease up temperature. Concentrations of U in melt decrease up temperature (Figure

313 5b) and are more sensitive to pressure than Th concentrations. The Th/U ratio of melt increases up

314 temperature until monazite exhaustion, after which it is relatively constant (Figure 5c). At low P, the

315 Th/U ratio of melt decreases at temperatures above monazite exhaustion.

316 The Th concentration of zircon in equilibrium follows the same trend as that of the melt, which

317 includes an increase up temperature and then decreases after monazite exhaustion (Figure 5d).

318 Concentrations of U in zircon decrease up temperature in a non-linear manner (Figure 5e). Contours of

319 the concentration of U in zircon are closer spaced at lower temperatures. Th/U values of zircon follow

320 the same general pattern as the Th/U ratio of melt with a maximum value at the monazite-out boundary.

321 After monazite exhaustion, the Th/U ratio of zircon decreases slightly up temperature (Figure 5f).

322 The sensitivity of the Th/U ratio of equilibrated zircon to the partition coefficient of Th between

323 monazite and melt, and the bulk concentrations of LREE, U, and Th are presented in Figure 6. Contours

324 on Figure 6 represent the P–T conditions where the modelled Th/U ratio of zircon is equal to 0.1. A

325 Th/U value of 0.1 has been proposed as a boundary between metamorphic and igneous zircon (e.g.

326 Hoskin & Schaltegger, 2003; Rubatto, 2017), although this Th/U value may not be appropriate as shown

327 by the dataset from Western Australia (Figure 1). A Th/U ratio of 0.1 occurs at lower temperatures for

14

328   low values of $D^{Th}_{mnz/melt}$ (Figure 6a). For very high $D^{Th}_{mnz/melt}$ values, a Th/U ratio of 0.1 for zircon

329   occurs near the monazite-out field boundary (Figure 6a).

330   Bulk rock concentrations of LREE are essentially a proxy for the amount of monazite present in

331   the system. For higher bulk concentrations of LREE, Th/U ratios of 0.1 of zircon occur at higher

332   temperatures (Figure 6b). For very low concentrations of LREE (e.g. 50 ppm), a Th/U ratio of 0.1 in

333   zircon occurs close to the muscovite-out field boundary. Moderate concentrations of LREE (e.g. 100–

334   200 ppm) result in a Th/U ratio of 0.1 of zircon at lower temperatures than biotite exhaustion at high

335   pressures and close to the biotite–cordierite field at low pressure. For high bulk rock concentrations of

336   LREE (500 ppm) a Th/U ratio of zircon of 0.1 is predicted to occur at UHT conditions.

337   Low bulk rock concentrations of U or high concentrations of Th result in Th/U ratios of zircon of

338   0.1 at relatively low temperatures (Figure 6c, d). High bulk rock concentrations of U or low

339   concentrations of Th result in Th/U ratios of 0.1 for zircon at relatively high temperatures (Figure 6c, d).

340   For most modelled bulk rock concentrations of U and Th, a Th/U ratio of 0.1 of zircon occurs between

341   the muscovite-out and biotite-out field boundaries (Figures 3 and 6c, d).

342

343   **4.4 Isobaric heating paths**

344   Results of the modelling for isobaric heating paths at 0.6 GPa and 0.9 GPa for the baseline scenario are

345   shown in Figures 7 and 8, respectively. The normalized molar proportions of the modelled phases

346   (approximately equivalent to volumetric proportions) are shown in Figures 7a and 8a. Melt production is

347   non-linear with temperature and there are punctuated increases in melt during the breakdown of

348   muscovite at low T (Figures 7a and 8a) and at 820°C for the 0.6 GPa heating path due to the breakdown

349   of biotite to cordierite (Figure 7a). The modelled concentration of Th in melt increases with heating and

350   reaches a maximum when monazite is exhausted (Figures 7b and 8b). After monazite is exhausted, the

351   amount of Th in the melt decreases due to dilution. In contrast, the U concentration of the melt decreases

352   along the entire heating path (Figures 7b and 8b). The proportion of each accessory mineral decreases

15

353   nearly exponentially with increasing temperature and all are completely exhausted by 950°C (Figures 7c

354   and 8c).

355   The modelled Th budget of the system at the solidus is dominated by monazite (~80%) but

356   decreases with increasing temperature (Figures 7d and 8d). After monazite exhaustion, the melt is the

357   dominant repository of Th (Figures 7d and 8d). In contrast to Th, the U budget of the system at the

358   solidus is nearly equally shared between accessory and major minerals (Figures 7e and 8e). Zircon

359   contains ~30% of the U budget, monazite contains ~20% and apatite ~2% at the solidus. With increasing

360   temperature, the amount of U hosted by the accessory and major minerals decreases with one important

361   exception. For the 0.6 GPa isobaric heating path, the U budget controlled by the major minerals

362   drastically increases at ~800°C (Figure 7e) – this is due to the growth of cordierite, which was modelled

363   with a $D^{U}_{cd/melt}$ value of 1.61 (Bea et al., 1994).

364   The modelled concentration of ThO_2 in monazite increases with temperature for both heating

365   paths (Figures 7f and 8f). After monazite exhaustion, the concentration of ThO_2 in monazite that would

366   be in equilibrium with the melt decreases during further heating. However, prograde or retrograde

367   monazite growth is not expected because the melt is predicted to be undersaturated in the LREE with

368   respect to monazite above the temperature of monazite exhaustion.

369   The modelled concentration of U in zircon decreases from >1,000 ppm to <1,000 ppm with

370   increasing temperature (Figures 7g and 8g). With increasing temperature, the modelled concentration of

371   Th in zircon initially decreases from ~200 ppm to ~100 ppm and then increases up to the temperature of

372   monazite exhaustion (Figures 7h and 8h). During heating for both modelled paths, the change of the

373   Th/U ratio of zircon is initially negligible followed by a non-linear increase in the Th/U ratio of zircon

374   until monazite is exhausted. After monazite exhaustion a gentle decrease in the Th/U ratio of zircon is

375   predicted (Figures 7i and 8i).

376

377   **4.5 Open system**

16

378   The results for an isobaric heating path at 0.9 GPa in an open system are summarized in Figure 9 along

379   with some of the comparative results for a closed system. The starting composition of the system is the

380   same as the baseline scenario for the closed system. The amount of melt generated in an open system is

381   less than the amount produced in a closed system scenario (Figures 8a and 9a). As a consequence, the

382   accessory minerals are stable to higher temperatures than in the closed system scenario (Figure 9b).

383   Roughly 50% of zircon, 85% of apatite and 25% of monazite are expected to survive heating up to

384   950°C.

385   Similar to the closed-system scenario, the modelled concentration of U in melt decreases with

386   heating (Figure 9c). The concentration of U in the system also decreases after each melt loss event

387   because the extracted melt has a higher concentration of U than the residue (Figure 9c). The

388   concentration of Th in the melt increases during the entire heating path (Figure 9d), which contrasts with

389   the decrease after monazite exhaustion in the closed system (Figure 8b). This is due to monazite

390   buffering the Th concentration of melt (and zircon) over the entire heating path. The concentration of Th

391   in the system increases and decreases during the heating path, which is due to the extracted melt having

392   both lower and higher concentrations of Th than the residue at each melt loss event (Figure 9d). The

393   concentration of P_2O_5 in melt increases after 750°C (Figure 9e) when the ASI value of the melt becomes

394   >1.1 and allows apatite dissolution in the modelling.

395   The predicted concentration of ThO_2 in monazite increases during heating, which is similar to

396   the closed system scenario. Modelled concentrations of U and Th in zircon and the Th/U ratio of zircon

397   are similar between open- and closed-system scenarios for the baseline scenario (Figure 9g–i).

398   The sensitivity of Th/U ratios of zircon to changes in the bulk rock concentrations of LREE, U

399   and the value of $D^{Th}_{mnz/melt}$ for an open system scenario are investigated in Figure 10. Low bulk rock

400   concentrations of LREE and U result in zircon with higher Th/U ratios (Figure 10a, b). Low values of

401    $D^{Th}_{mnz/melt}$ result in zircon with higher Th/U ratios (Figure 10c). These are similar to the results for the

402   closed system scenario (Figure 6b).

17

403

404 **5 DISCUSSION**

405 **5.1 Limitations and assumptions of modelling**

406 There are several key assumptions in the modelling, including the following factors: (1) there are no

407 kinetic barriers to the dissolution of accessory minerals, (2) there are no other accessory minerals (e.g.

408 xenotime, allanite) in the system, (3) LREE, Zr and P do not substitute into the major rock-forming

409 minerals, (4) Th substitution in accessory minerals follows Henrian behaviour, (5) rock-wide chemical

410 and thermal equilibration is achieved, (6) apatite is unreactive in the high-P and low-T portion of the

411 modelled system (i.e. when the ASI value of the modelled melt is <1.1), and (7) no adjustment was

412 made to concentration of Ca in the model metapelite to account for apatite.

413 First, the modelling assumes that there are no kinetic barriers to dissolution and crystallization

414 during suprasolidus metamorphism. For accessory minerals, the time required to dissolve grains of

415 zircon (Harrison and Watson, 1983), monazite (Harrison & Watson, 1984) and apatite (Rapp & Watson,

416 1986) are summarized in Figure 11. The dissolution of these phases is sensitive to temperature, the

417 amount of H_2O in the melt and the deviation from saturation (Watson, 1996). For the average metapelite

418 composition modelled here, H_2O concentrations in melt range from ~10 wt.% at the wet solidus down to

419 ~3 wt.% at UHT conditions. There is no significant difference between the H_2O concentration of melt

420 between the open and closed system scenarios. In general, there is not expected to be any significant

421 kinetic barriers to dissolution over orogenic timescales (>1 My). For systems with a realistic 6 wt.%

422 H_2O in the melt, the time required to completely dissolve zircon, monazite and apatite is less than 100

423 ky to 1 My for the grain sizes considered (Figure 11a–c). In a completely dry system, apatite dissolution

424 may be hindered (Figure 11a). Nonetheless, apatite is not a major contributor to the Th and U budget of

425 the system and is not expected to significantly influence the Th/U ratio of metamorphic zircon.

426 A second limitation of the modelling is that it does not consider the influence of other accessory

427 minerals that can host significant quantities of Th and U, including allanite and xenotime (e.g. Engi,

18

428 2017). However, the modelled composition is representative of an aluminous metapelite at suprasolidus

429 conditions and allanite is not expected to be stable (e.g. Spear, 2010; Wing et al., 2003). Xenotime is a

430 common mineral in subsolidus pelites, but phase equilibria modelling of xenotime and monazite

431 suggests that xenotime is completely consumed at temperatures just above the solidus (Spear & Pyle,

432 2010), at least in those rock compositions. Xenotime abundance in natural high-temperature granulites is

433 typically lower than monazite and zircon, largely because xenotime and garnet have an inverse

434 abundance relationship (e.g. Spear & Pyle, 2010). Therefore, for the modelled composition and P–T

435 conditions, allanite and xenotime are not expected to be stable in the equilibrium assemblage above the

436 solidus. For other compositions, such as Ca-rich metapelites, the influence of allanite on the Th/U ratios

437 of zircon may need to be considered especially at subsolidus conditions (e.g. Finger et al., 2016; Janots

438 et al., 2008). However, subsolidus zircon growth is considered to be much less significant and

439 voluminous than suprasolidus zircon growth.

440   A third limitation of the modelling is that the essential structural constituents of zircon, monazite

441 and apatite (Zr, LREE and P) are assumed to reside only in the accessory minerals and do not substitute

442 into major minerals. Apatite and monazite are the main repositories of P in suprasolidus metamorphic

443 rocks, but feldspar and garnet can accommodate significant amounts of P (Pyle & Spear, 1999;

444 Villaseca, Martín Romera, De la Rosa, & Barbero, 2003; Kohn & Malloy, 2004; Dumond, Gonclaves,

445 Williams, & Jercinovic, 2015). In most cases, garnet is likely to contain up to a few hundred ppm of P,

446 but extreme concentrations of up to 0.4 wt.% P_2O_5 have been documented in some ultrahigh-temperature

447 metamorphic rocks (Axler & Ague, 2015a, 2015b). In the modelling here, consider a maximum garnet

448 mode of 20 vol.%, and a concentration of 250 ppm P in garnet (e.g. Dumond et al., 2015). A simple

449 mass balance calculation with the apatite and monazite proportions at the solidus will result in garnet

450 hosting ~7% of the P_2O_5 budget. Villaseca et al. (2003) reported concentrations of P_2O_5 in feldspar of

451 0.18–0.22 wt.%. Considering 20 vol. % feldspar with apatite and monazite modes at the solidus, the

452 result is that feldspar could host 15% of the P_2O_5 budget. In both of these scenarios, the incorporation of

453   P into major minerals will reduce the *effective concentration* (c.f. Kelsey et al., 2008) of P in the system

454   allocated to form apatite and monazite (e.g. Yakymchuk, 2017), which will result in a slightly decreased

455   stability field of monazite. In the baseline scenario in this study (Figure 5), zircon could therefore attain

456   Th/U ratios >0.1 at slightly lower temperatures if P substitution is considered.

457   Zirconium can readily substitute into rutile and to a lesser extent into garnet (e.g. Bea et al.,

458   2006; Kohn, Corrie, & Markley, 2015). The substitution of Zr into minerals other than zircon reduces

459   the effective concentration of Zr in the system and results in a reduced stability field of zircon. For

460   example, rutile can accommodate up to a few thousand ppm Zr at UHT conditions (e.g. Tomkins,

461   Powell, & Ellis, 2007). Considering the maximum proportion of rutile in the modelled metapelite

462   composition (~0.2 mol.%), and a concentration of 5,000 ppm Zr in rutile, and a bulk composition of 150

463   ppm Zr, the result is that ~6% of the bulk rock Zr can be locked in rutile. Garnet can accommodate

464   hundreds of ppm of Zr at UHT conditions, which may be more important. For example, consider an

465   average metapelite with 20 vol.% garnet with an extreme Zr concentration of 100 ppm (e.g. Kohn et al.,

466   2015) and a bulk rock Zr concentration of 150 ppm. The result is that ~11% of the Zr will be locked

467   away in garnet. Again this will slightly reduce the stability field of zircon. However, zircon contains

468   only up to 20% of the U budget of the rock (e.g. Figures 7e and 8e) and a negligible proportion of the Th

469   budget (Figures 7d and 8d). Because of the relatively small influence of zircon on the Th and U

470   concentrations of melt, the role of Zr substitution into major minerals is expected to have a negligible

471   effect on the Th/U ratio of equilibrated zircon.

472   The impact of LREE substitution into major minerals is potentially more important because the

473   amount of monazite in equilibrium with melt and zircon has a significant impact on the Th budget of the

474   system and the Th/U ratio of equilibrated zircon. In peraluminous migmatites investigated by Bea

475   (1996), feldspar contained roughly 5% of the LREE budget of samples and apatite 10%. The partitioning

476   of LREE into apatite is considered in the models here (e.g. Yakymchuk, 2017) and apatite contains up to

477   30% of the LREE budget in the modelled accessory minerals. LREE substitution in feldspar is not

478   considered in the models here, but if feldspar contains 20 ppm LREE (the average of values reported in

479   Bea, 1996) and a mode of 20 vol.% (the maximum in the modelling here), this accounts for ~7% of the

480   LREE budget of a rock with a bulk concentration of 150 ppm LREE. The result is a slightly lower

481   effective concentration of LREE allocated to monazite and less monazite will be present in the system to

482   partition Th. Consequently, the modelled Th/U ratio in equilibrated zircon is expected to be slightly

483   higher (e.g. Figure 10a) than for a system where LREE substitution into feldspar is not considered.

484   The fourth assumption is that concentrations of Th and U in major and accessory minerals can be

485   modelled by partition coefficients and conform to Henry's law. For the major minerals, zircon, and

486   apatite this is likely a valid assumption due to the very low concentrations of Th and U in these minerals.

487   Because Th can substitute into monazite in higher concentration than zircon and apatite, Th partitioning

488   into monazite may depart from Henrian behaviour towards Raoultian behaviour. This has been discussed

489   in detail for experimental results of monazite stability in Skora and Blundy (2010). The consequences

490   for the modelling here are relatively minor because most modelled monazite has low concentrations of

491   Th and Henrian behaviour is likely (Figures 7d and 8d). Modelled ThO_2 concentrations in monazite can

492   reach ~30 wt.% at high temperature (i.e. Th becomes an essential structural constituent in monazite), but

493   this occurs when monazite proportions are approaching zero.

494   The partition coefficients for Th between monazite and melt vary significantly between experimental

495   studies of natural samples and experiments (Figure 2). Starting compositions of the experimental studies

496   have Th concentrations ranging between 216 and 1063 ppm (Hermann & Rubatto, 2009; Skora &

497   Blundy, 2010; Stepanov et al., 2012; Xing et al., 2013), which are one to two orders of magnitude more

498   than concentrations of Th in most peraluminous granites and metasedimentary rocks. Thorium

499   substitution into monazite may be limited by the substitution mechanism. Direct substitution of

500   tetravalent Th with the formation of vacancies limits the amount of ThO_2 in monazite to ~18 wt.%

501   whereas coupled substitution of Th with Ca can account for up to ~30 wt.% ThO_2 (e.g. Clavier, Podor &

502   Dacheux., 2011). The concentration of Th in monazite from natural samples and experiments have the

503   same general range of values even though the melt compositions are highly variable (Figure 2).

504   Considering the high-Th compositions of the starting materials and melts in experimental studies, we

505   speculate that the amount of Th incorporated into monazite may be limited by these substitution

506   mechanisms and that the partition coefficients derived from co-existing Th-rich melt and monazite in

507   experimental runs may be underestimates.

508   The fifth assumption of this modelling is that minerals are expected to be in equilibrium with each

509   other (and anatectic melt) and are compositionally homogeneous throughout the rock. In natural

510   systems, most major and accessory minerals preserve some compositional zoning and inclusions are

511   chemically isolated from matrix. Apatite zoning in metamorphic rocks has been documented (e.g. Yang

512   & Rivers, 2002) and chemical zoning in monazite is ubiquitous and used to infer different portions of

513   the metamorphic history (e.g. Engi, 2017; Williams, Jercinovic, & Hetherington, 2007). In suprasolidus

514   metamorphic rocks, zircon that grew from anatectic melt is generally weakly zoned in

515   cathodoluminescence images (e.g. Rubatto, 2017). However, it is clear from studies of REE partitioning

516   between melt, garnet and zircon that equilibrium in trace elements between major and accessory

517   minerals can be a reasonable approximation (e.g. Taylor, Kirkland, & Clark, 2016; Rubatto, 2017). This

518   is the basis for most studies in petrochronology, although there are clear cases where equilibrium was

519   not attained between accessory and major minerals in metamorphic systems (e.g. Lanari & Engi, 2017).

520   The sixth limitation is that we assume apatite is unreactive when the ASI value of the melt is less

521   than 1.1. Modelled melt ASI values <1.1 are found at < 660°C at 8 kbar and <850°C at 12 kbar (c.f.

522   Yakymchuk, 2017) where melt modes are less than 30 mol.% in closed system (Figure 4a). Apatite is

523   expected to contain a very small portion of the Th and U budgets of the system (e.g. Figures 7d, e and

524   8d, e) and is expected to have a negligible effect on zircon Th/U ratios in the portion of P–T space where

525   we assume apatite is unreactive.

526   The seventh and final assumption of the modelling is that we do not adjust the concentration of

527   Ca in the bulk system to account for apatite. The amount of Ca that would be needed to be subtracted

528   from the bulk composition to account for apatite is a function of the concentrations of the essential

529   structural constituents of apatite (P) and monazite (LREE, P). For the scenarios presented here,

530   monazite only requires a negligible amount of P (e.g. Yakymchuk, 2017). Approximately 0.25 wt.% of

531   CaO would need to be subtracted from the average metapelite composition at the solidus to account for

532   CaO in apatite, but this amount would vary based on the amount of apatite (and monazite) dissolution in

533   closed- and open-system scenarios. Although slight changes in the phase boundaries are expected, the

534   amount of Th and U in the major phases is relatively small, and this is not expected to have a significant

535   effect on the modelled Th/U ratios in zircon.

536

537   **5.2 Controls on Th/U ratios of zircon in suprasolidus metamorphic rocks**

538   The modelling here suggests that there are two major controls on the Th/U of zircon in equilibrium with

539   anatectic melt in an average metapelite in closed and open systems. These include: (1) the Th/U ratio

540   and concentrations of Th and U in the system, and (2) the growth and breakdown of monazite.

541   In an equilibrated system, the concentration of Th and U in the melt is controlled by the modes of the

542   major and accessory minerals, the partition coefficients and the concentrations of Th and U in the

543   system. The concentrations of Th and U in fine-grained sedimentary rocks are variable, but generally

544   have Th/U ratios of 3.5–5.5 (McLennan, Taylor, & Hemming, 2006) with some modern sediments

545   recording extreme values of 1.0 to >6.0 (McLennan & Taylor, 1991). Post-Archean fine-grained

546   sedimentary rocks have U concentrations of around 3.0–3.5ppm and Th concentrations of about 12–16

547   ppm (Condie, 1993; McLennan et al., 2006). These are also broadly equivalent to the concentrations of

548   these elements in the upper continental crust (e.g. Rudnick & Gao, 2014). However, some pelites can

549   have values that depart from these. Shales with elevated U concentrations, such as those found in

550   reducing environments (e.g. black shales), will generally have low Th/U ratios (e.g. Taylor &

551   McLennan, 1991) and would result in metamorphic zircon with relatively low Th/U ratios. Sediments

552   derived from juvenile sources with low Th/U, such as oceanic island basalts, can be found in back-arc

23

553   basins (McLennan, Taylor, McCulloch, & Maynard, 1990). Finally, post-depositional leaching of U

554   and/or Th of sedimentary rocks may also contribute to the Th/U of metamorphic zircon.

555   The breakdown and growth of monazite above the solidus is an important control on Th/U ratios in

556   suprasolidus metamorphic zircon. When melt composition is buffered by monazite, Th partitions mostly

557   between it and anatectic melt (Figures 7d and 8d). Consequently, zircon in equilibrium with monazite

558   and melt will generally have low Th/U ratios. This was proposed in many studies of zircon from high-

559   temperature metapelites and S-type granites (e.g. Cesare et al., 2003; Rubatto et al., 2001; Vavra et al.,

560   1996). As monazite is consumed, the Th concentration of the melt increases (Figures 5a, 7b, 8b and 9d),

561   which results in equilibrated zircon with increasing Th/U values during heating (Figures 7i, 8i and 9i).

562   When monazite is completely exhausted, the Th/U ratio of equilibrated zircon reaches a maximum

563   (Figures 5–10). Because monazite is the primary repository for Th in the modelling here (Figure 7d and

564   8d), further melting will dilute the melt in Th. Less dilution of U occurs because a larger proportion of U

565   is hosted in the major minerals (Figures 7e and 8e). Consequently, the Th/U ratio of equilibrated zircon

566   decreases after the exhaustion of monazite (Figures 5–10).

567   This modelling evaluates the composition of zircon in equilibrium with anatectic melt over a range

568   of *P–T* conditions, but zircon is generally expected to crystallize during cooling to the solidus (Kelsey et

569   al., 2008; Kohn et al., 2015; Yakymchuk & Brown, 2014b; Yakymchuk et al., 2017). If zircon

570   continuously re-equilibrates its Th/U ratio during cooling to the solidus, then the ratio that is preserved

571   in the zircon will be that at the solidus unless further re-equilibration occurs at subsolidus conditions.

572   However, given the low diffusivity of Th and U in zircon (e.g. Cherniak, Hanchar & Watson, 1997), it is

573   more likely that the zircon will record a range of Th/U values where the cores record early Th/U ratios

574   in the crystallization history and the rims record values near the solidus. This is not explored in the

575   modelling here, but considering that zircon is a relatively minor contributor to the U and Th budget of

576   the system (Figures 7d,e, and 8d, e), the fractionation of Th and U in early grown zircon is not expected

577   to have a major impact on the Th/U ratio of later grown zircon. Nonetheless, a range of Th/U values is

578   expected to be recorded in newly grown anatectic zircon in natural systems.

579   For the equilibrium closed system scenarios modelled here, the Th/U locked into the zircon is

580   expected to be the value where the retrograde path crosses the wet solidus. For most of the modelled

581   variables, this results in zircon with Th/U ratios <0.1, except at $D^{Th}_{mnz/melt}$ values <3,000 (Figure 6a) or

582   very low concentrations of U (Figure 6c) or very high concentrations of Th (Figure 6d). Migmatites with

583   large proportions of leucosome may reflect approximately closed system behaviour where melt did not

584   escape and these rocks commonly contain metamorphic zircon with Th/U ratios <0.1 (Gasser et al.,

585   2012; Rubatto et al., 2009; Rubatto et al., 2013; Rubatto, 2017). This likely reflects the relatively low

586   temperature of zircon crystallization at or near the wet solidus where zircon Th/U ratios are expected to

587   be <0.1 (Figures 5–8).

588   In an open system, the extraction of melt elevates the temperature of the solidus (e.g. White &

589   Powell, 2002; White et al., 2007) and the Th/U ratio of the zircon is predicted to be locked in at

590   temperatures higher than the wet solidus. The actual temperature of the solidus will be influenced by the

591   amount of melt extracted from the system, but in the modelling here, it occurs at ~5–20°C below the last

592   melt loss event reached along the modelled isobaric heating path (Figure 10). For all the modelled

593   scenarios, the highest Th/U ratio in zircon is predicted at the solidus for the highest-temperature melt

594   loss event. For most modelled scenarios, UHT conditions are associated with Th/U ratios in zircon >0.1.

595   This is consistent with the results from residual metapelites in the Eastern Ghats (Korhonen et al., 2013),

596   the lower crust in the Ivrea zone (Ewing, Hermann, & Rubatto, 2013; Vavra et al., 1996) and crustal

597   rocks from the Musgrave Province, Central Australia (Howard et al., 2015; Smithies et al., 2011).

598   The relative timing of monazite and zircon growth during cooling and crystallization of anatectic

599   melt is also an important control in open-system scenarios. Upon cooling, if monazite crystallizes close

600   to the solidus (c.f. Kelsey et al., 2008), initial suprasolidus metamorphic zircon is expected to have high

601   Th/U ratios and late crystallized zircon that grows in the presence of monazite is predicted to have low

602   Th/U ratios. This is particularly important for rocks with low concentrations of LREE (e.g. Yakymchuk

603   & Brown, 2014b). A similar sequence of Th/U ratios of zircon was documented by Hokada and Harley

604   (2004) in the Napier complex where zircon cores with Th/U> 1 formed during crystallization of the

605   leucosomes and zircon rims with Th/U<1 formed in the presence of monazite late in the crystallization

606   history. In scenarios where zircon and monazite co-precipitate during cooling, such as in systems

607   relatively that are enriched in LREE, then all newly crystallized anatectic zircon is expected to have

608   relatively low Th/U ratios.

609

610   **5.3 Th/U ratios of zircon in metamorphic rocks**

611   Previous compilations of zircon Th/U ratios have proposed a general threshold Th/U value of 0.1

612   between metamorphic and igneous zircon (e.g. Hoskin & Schaltegger, 2003; Rubatto, 2017). Based on

613   the new compilation of zircon analyses from Western Australia, it is more appropriate to say that

614   igneous zircon rarely have Th/U < 0.1 and that metamorphic zircon can have values ranging from <0.01

615   to >10 (Figure 1a). Therefore, zircon with Th/U ratios <0.1 are more likely to be metamorphic and

616   zircon with Th/U ratios >0.1 can be igneous or metamorphic. The results of the modelling here suggest

617   that one of the primary controls on the Th/U ratio of zircon in metamorphic rocks is the presence and

618   proportion of Th-rich monazite. Considering that the database contains zircon from different rock types

619   at various $P–T$ conditions, the breakdown and growth of other Th-rich minerals may also have a similar

620   influence on the Th budget of the rock and the Th/U ratio of equilibrated zircon.

621   In rocks with high-Ca bulk compositions (e.g. metabasites and calc-silicate rocks), allanite is a

622   common accessory mineral and is a major repository for Th (Hermann, 2002; Engi, 2017). Allanite is

623   expected to grow from the breakdown of lawsonite and titanite—also relatively Th-rich minerals—

624   during prograde high dP/dT metamorphism (Spandler, Hermann, Arculus & Mavrogenes, 2003) and

625   also may be partly consumed during high-temperature partial melting (e.g. Klimm, Blundy & Green,

626   2008). Although the Th/U ratio of equilibrated zircon in these systems will be dependent on the mode of

627   allanite (or other Th-rich minerals), zircon is generally expected to have low Th/U ratios in allanite-

628   bearing systems (Rubatto, 2017).

629   At subsolidus conditions, the proportion of monazite in metapelites is expected to increase during

630   prograde metamorphism and reach a maximum at the solidus (Spear and Pyle, 2010). While subsolidus

631   prograde zircon growth is not generally expected (c.f. Kohn et al., 2015), any new or recrystallized

632   zircon would be expected to have relatively low Th/U ratios near the solidus and higher Th/U ratios at

633   lower temperatures if there are no additional Th-rich minerals present. In Ca-rich pelites, allanite may be

634   present at lower temperatures than monazite (e.g. Janots et al., 2007; Spear, 2010) and equilibrated

635   zircon is also expected to have relatively low Th/U ratios. However, the Th/U ratio of equilibrated

636   zircon will be significantly influenced by the proportion of Th-rich minerals, which is in part controlled

637   by the bulk composition of the system and the availability of the essential structural constituents of these

638   minerals.

639

640   **6 CONCLUSIONS**

641   A compilation of metamorphic zircon from Western Australia yields a range of values with a median of

642   0.4. This median Th/U ratio is higher than 0.1, which is commonly used to separate metamorphic from

643   igneous zircon. Based on phase equilibria modelling, for closed system scenarios, low-temperature

644   crystallization of zircon at or near the wet solidus is likely to lead to Th/U ratios <0.1. However, for

645   open system melting, melt loss will result in elevated solidus temperatures and zircon is predicted to

646   have higher Th/U ratios. Under UHT conditions zircon is expected to have Th/U ratios >0.1. The main

647   controls on the Th/U ratio of suprasolidus metamorphic zircon are (1) the Th/U ratio and concentrations

648   of Th and U in the system, (2) the amount of monazite in the system, which is a function of the

649   concentration of LREE and the amount of melt in the system. Crystallization timing is also likely to be a

650   strong control on zircon grain Th/U ratio; high Th/U ratios are expected early during cooling and melt

651   crystallization in the absence of monazite. By contrast, low Th/U ratios in zircon are expected to occur

652   late in the cooling and crystallization history near the solidus and in the presence of monazite.

653

654   **ACKNOWLEDGEMENTS**

660 **REFERENCES**

661 Acosta-Vigil, A., Buick, I., Hermann, J., Cesare, B., Rubatto, D., London, D., & Morgan, G. B. (2010).

662   Mechanisms of Crustal Anatexis: a Geochemical Study of Partially Melted Metapelitic Enclaves

663   and Host Dacite, SE Spain. *Journal of Petrology*, 51, 785–821.

664 Ague, J. J. (1991). Evidence for major mass transfer and volume strain during regional metamorphism

665   of pelites. *Geology*, 19, 855–858.

666 Axler, J. A., & Ague, J. J. (2015a). Exsolution of rutile or apatite precipitates surrounding ruptured

667   inclusions in garnet from UHT and UHP rocks. *Journal of Metamorphic Geology*, 33, 829–848.

668 Axler, J. A., & Ague, J. J. (2015b). Oriented multiphase needles in garnet from ultrahigh-temperature

669   granulites, Connecticut, U.S.A. *American Mineralogist*, 100, 2254–2271.

670 Ayres, M., & Harris, N. (1997). REE fractionation and Nd-isotope disequilibrium during crustal

671   anatexis: constraints from Himalayan leucogranites. *Chemical Geology*, 139, 249–269.

672 Bea, F. (1996). Residence of REE, Y, Th and U in Granites and Crustal Protoliths; Implications for the

673   Chemistry of Crustal Melts. *Journal of Petrology*, 37, 521–552.

674 Bea, F., & Montero, P. (1999). Behavior of accessory phases and redistribution of Zr, REE, Y, Th, and

675   U during metamorphism and partial melting of metapelites in the lower crust: an example from

676   the Kinzigite Formation of Ivrea-Verbano, NW Italy. *Geochimica et Cosmochimica Acta*, 63,

677   1133–1153.

678 Bea, F., Pereira, M. D., & Stroh, A. (1994). Mineral/leucosome trace-element partitioning in a

679   peraluminous migmatite (a laser ablation-ICP-MS study). *Chemical Geology*, 117, 291–312.

680 Bea, F., Montero, P., & Ortega, M. (2006). A LA-ICP-MS evaluation of Zr reservoirs in common crustal

681   rocks: implications for Zr and Hf geochemistry, and zircon-forming processes. *The Canadian

682   Mineralogist*, 44, 693–714.

683 Boehnke, P., Watson, E. B., Trail, D., Harrison, T. M., & Schmitt, A. K. (2013). Zircon saturation re-

684   revisited. *Chemical Geology*, 351, 324–334.

685   Breiter, K. (2016). Monazite and zircon as major carriers of Th, U, and Y in peraluminous granites:

686   examples from the Bohemian Massif. *Mineralogy and Petrology*, 110, 767–785.

687   Brown, M. (2013). Granite: From genesis to emplacement. *Geological Society of America Bulletin*, 125,

688   1079–1113.

689   Cesare, B., Gómez-Pugnaire, M. T., & Rubatto, D. (2003). Residence time of S-type anatectic magmas

690   beneath the Neogene Volcanic Province of SE Spain: a zircon and monazite SHRIMP study.

691   *Contributions to Mineralogy and Petrology*, 146, 28–43.

692   Cherniak, D. J., Hanchar, J. M. & Watson, E. B. (1997). Diffusion of tetravalent cations in zircon.

693   *Contributions to Mineralogy and Petrology*, 127, 383–390.

694   Clavier, N., Podor, R. & Dacheux, N. (2011). Crystal chemistry of the monazite structure. *Journal of the*

695   *European Ceramic Society*, 31, 941–976.

696   Clemens, J. D. (2006). Melting of the continental crust: fluid regimes, melting reactions, and source-

697   rock fertility. In: Brown, M., & Rushmer, T. (eds). Evolution and differentiation of the

698   Continental Crust. Cambridge: Cambridge University Press. pp 296–330.

699   Condie, K. C. (1993). Chemical composition and evolution of the upper continental crust: Contrasting

700   results from surface samples and shales. *Chemical Geology*, 104, 1–37.

701   Diener, J. F. A., White, R. W., & Powell, R. (2008). Granulite facies metamorphism and subsolidus

702   fluid-absent reworking, Strangways Range, Arunta Block, central Australia. *Journal of*

703   *Metamorphic Geology*, 26, 603–622.

704   Duc-Tin, Q., & Keppler, H. (2015). Monazite and xenotime solubility in granitic melts and the origin of

705   the lanthanide tetrad effect. *Contributions to Mineralogy and Petrology*, 169, 1–26.

706   Dumond, G., Goncalves, P., Williams, M.L., & Jercinovic, M.J. (2015). Monazite as a monitor of

707   melting, garnet growth and feldspar recrystallization in continental lower crust. *Journal of*

708   *Metamorphic Geology*, 33, 735–762.

709   Engi, M. (2017). Petrochronology Based on REE-Minerals: Monazite, Allanite, Xenotime, Apatite.

710   *Reviews in Mineralogy and Geochemistry*, 83, 365–418.

711   Ewing, T. A., Hermann, J., & Rubatto, D. (2013). The robustness of the Zr-in-rutile and Ti-in-zircon

712   thermometers during high-temperature metamorphism (Ivrea-Verbano Zone, northern Italy).

713   *Contributions to Mineralogy and Petrology*, 165, 757–779.

714   Finger, F., Krenn, E., Schulz, B., Harlov, D., & Schiller, D. (2016). "Satellite monazites" in

715   polymetamorphic basement rocks of the Alps: Their origin and petrological significance.

716   *American Mineralogist*, 101, 1094–1103.

717   Förster, H.-J. (1998). The chemical composition of REE-Y-Th-U-rich accessory minerals in

718   peraluminous granites of the Erzgebirge-Fichtelgebirge region, Germany; Part I, The monazite-

719   (Ce)-brabantite solid solution series. *American Mineralogist*, 83, 259–272.

720   Guernina, S., & Sawyer, E. W. (2003). Large-scale melt-depletion in granulite terranes: an example

721   from the Archean Ashuanipi Subprovince of Quebec. *Journal of Metamorphic Geology*, 21,

722   181–201.

723   Guevara, V., & Caddick, M. (2016). Shooting at a moving target: phase equilibria modelling of high‐

724   temperature metamorphism. *Journal of Metamorphic Geology*, 34, 209–235.

725   Hanson, G. N. (1978). The application of trace elements to the petrogenesis of igneous rocks of granitic

726   composition. *Earth and Planetary Science Letters*, 38, 26-43.

727   Harley, S. L., Kelly, N. M., & Möller, A. (2007). Zircon Behaviour and the Thermal Histories of

728   Mountain Chains. *Elements*, 3, 25–30.

729   Harrison, T. M., & Watson, E. B. (1983). Kinetics of zircon dissolution and zirconium diffusion in

730   granitic melts of variable water content. *Contributions to Mineralogy and Petrology*, 84, 66–72.

731   Harrison, T. M., & Watson, E. B. (1984). The behavior of apatite during crustal anatexis: equilibrium

732   and kinetic considerations. *Geochimica et Cosmochimica Acta*, 48, 1467–1477.

733 Hermann, J. (2002). Allanite: thorium and light rare earth element carrier in subducted crust. *Chemical*

734   *Geology*, 192, 289–306.

735 Hermann, J., & Rubatto, D. (2009). Accessory phase control on the trace element signature of sediment

736   melts in subduction zones. *Chemical Geology*, 265, 512–526.

737 Holland, T. J. B., & Powell, R. (2011). An improved and extended internally consistent thermodynamic

738   dataset for phases of petrological interest, involving a new equation of state for solids. *Journal of*

739   *Metamorphic Geology*, 29, 333–383.

740 Hoskin, P. W., & Schaltegger, U. (2003). The composition of zircon and igneous and metamorphic

741   petrogenesis. *Reviews in mineralogy and geochemistry*, 53, 27–62.

742 Howard, H. M., Smithies, R. H., Kirkland, C. L., Kelsey, D. E., Aitken, A., Wingate, M. T. D., ... Maier,

743   W. D. (2015). The burning heart — The Proterozoic geology and geological evolution of the

744   west Musgrave Region, central Australia. *Gondwana Research*, 27, 64–94.

745 Inger, S., & Harris, N. (1993). Geochemical Constraints on Leucogranite Magmatism in the Langtang

746   Valley, Nepal Himalaya. *Journal of Petrology*, 34, 345–368.

747 Janots, E., Engi, M., Berger, A., Allaz, J., Schwarz, J. O., & Spandler, C. (2008). Prograde metamorphic

748   sequence of REE minerals in pelitic rocks of the Central Alps: implications for allanite–

749   monazite–xenotime phase relations from 250 to 610 C. *Journal of Metamorphic Geology*, 26,

750   509–526.

751 Johnson, T. E., Clark, C., Taylor, R. J., Santosh, M., & Collins, A. S. (2015). Prograde and retrograde

752   growth of monazite in migmatites: An example from the Nagercoil Block, southern India.

753   *Geoscience Frontiers*, 6, 373–387.

754 Kelly, N. M., & Harley, S. L. (2005). An integrated microtextural and chemical approach to zircon

755   geochronology: refining the Archaean history of the Napier Complex, east Antarctica.

756   *Contributions to Mineralogy and Petrology*, 149, 57–84.

757   Kelsey, D. E., Clark, C., & Hand, M. (2008). Thermobarometric modelling of zircon and monazite

758   growth in melt-bearing systems: examples using model metapelitic and metapsammitic

759   granulites. *Journal of Metamorphic Geology*, 26, 199–212.

760   Kelsey, D. E., & Powell, R. (2011). Progress in linking accessory mineral growth and breakdown to

761   major mineral evolution in metamorphic rocks: a thermodynamic approach in the Na2O-CaO-

762   K2O-FeO-MgO-Al2O3-SiO2-H2O-TiO2-ZrO2 system. *Journal of Metamorphic Geology*, 29,

763   151–166.

764   Kelsey, D. E., & Hand, M., (2015). On ultrahigh temperature crustal metamorphism: phase equilibria,

765   trace element thermometry, bulk composition, heat sources, timescales and tectonic settings.

766   Geoscience Frontiers, 6, 311–356.

767   Kirkland, C. L., Smithies, R. H., Taylor, R. J. M., Evans, N. & McDonald, B. (2015). Zircon Th/U ratios

768   in magmatic environs. *Lithos*, 212, 397–414.

769   Klemme, S., Günther, D., Hametner, K., Prowatke, S., & Zack, T. (2006). The partitioning of trace

770   elements between ilmenite, ulvospinel, armalcolite and silicate melts with implications for the

771   early differentiation of the moon. *Chemical Geology*, 234, 251–263.

772   Klemme, S., Prowatke, S., Hametner, K., & Günther, D. (2005). Partitioning of trace elements between

773   rutile and silicate melts: Implications for subduction zones. *Geochimica et Cosmochimica Acta*,

774   69, 2361–2371.

775   Klimm, K., Blundy, J. D. & Green, T. H. (2008). Trace Element Partitioning and Accessory Phase

776   Saturation during H2O-Saturated Melting of Basalt with Implications for Subduction Zone

777   Chemical Fluxes. *Journal of Petrology*, 49, 523–553.

778   Kohn, M. J., Corrie, S. L., & Markley, C. (2015). The fall and rise of metamorphic zircon. *American*

779   *Mineralogist*, 100, 897–908.

780   Kohn, M. J., & Malloy, M. A. (2004). Formation of monazite via prograde metamorphic reactions

781   among common silicates: implications for age determinations. *Geochimica et Cosmochimica*

782   *Acta*, 68, 101–113.

783   Korhonen, F.J., Clark, C., Brown, M., Bhattacharya, S., & Taylor, R. (2013). How long-lived is

784   ultrahigh temperature (UHT) metamorphism? Constraints from zircon and monazite

785   geochronology in the Eastern Ghats orogenic belt, India. *Precambrian Research*, 234, 322–350.

786   Korhonen, F. J., Saito, S., Brown, M., Siddoway, C. S., & Day, J. M. D. (2010). Multiple Generations of

787   Granite in the Fosdick Mountains, Marie Byrd Land, West Antarctica: Implications for

788   Polyphase Intracrustal Differentiation in a Continental Margin Setting. *Journal of Petrology*, 51,

789   627–670.

790   Lanari, P., & Engi, M. (2017). Local Bulk Composition Effects on Metamorphic Mineral Assemblages.

791   *Reviews in Mineralogy and Geochemistry*, 83, 55–102.

792   Mahood, G., & Hildreth, W. (1983). Large partition coefficients for trace elements in high-silica

793   rhyolites. *Geochimica et Cosmochimica Acta*, 47, 11–30.

794   Mayne, M. J., Moyen, J. F., Stevens, G., & Kaisl Aniemi, L. (2016). Rcrust: a tool for calculating path‐

795   dependent open system processes and application to melt loss. *Journal of Metamorphic Geology,*

796   34, 663–682.

797   McLennan, S. M., & Taylor, S. R. (1991). Sedimentary Rocks and Crustal Evolution: Tectonic Setting

798   and Secular Trends. *The Journal of Geology*, 99, 1–21.

799   McLennan, S. M., Taylor, S. R., & Hemming, S. R. (2006). Composition, differentiation, and evolution

800   of continental crust: constraints from sedimentary rocks and heat flow. In: Evolution and

801   Differentiation of the Continental Crust (eds Brown, M. & Rushmer, T.). Cambridge: Cambridge

802   University Press. pp 92–134.

803 McLennan, S. M., Taylor, S. R., McCulloch, M. T., & Maynard, J. B. (1990). Geochemical and Nd-Sr

804   isotopic composition of deep-sea turbidites: Crustal evolution and plate tectonic associations.

805   *Geochimica et Cosmochimica Acta*, 54, 2015–2050.

806 Montel, J.-M. (1993). A model for monazite/melt equilibrium and application to the generation of

807   granitic magmas. *Chemical Geology*, 110, 127–146.

808 Nash, W. P., & Crecraft, H. R. (1985). Partition coefficients for trace elements in silicic magmas.

809   *Geochimica et Cosmochimica Acta*, 49, 2309–2322.

810 Pichavant, M., Herrera, J. V., Boulmier, S., Briqueu, L., Joron, J.-L., Juteau, M., ... Treuil, M. (1987).

811   The Macusani glasses, SE Peru: evidence of chemical fractionation in peraluminous magmas. In:

812   Myson, B.O. (ed.) Magmatic Processes: Physicochemical Principles. University Park,

813   Pennsylvania: Geochemical Society. 359–373,

814 Powell, R., & Holland, T. J. B. (1988). An internally consistent dataset with uncertainties and

815   correlations: 3. Applications to geobarometry, worked examples and a computer program.

816   *Journal of Metamorphic Geology*, 6, 173–204.

817 Prowatke, S., & Klemme, S. (2006). Trace element partitioning between apatite and silicate melts.

818   *Geochimica et Cosmochimica Acta*, 70, 4513–4527.

819 Pyle, J. M., & Spear, F. S. (1999). Yttrium zoning in garnet: coupling of major and accessory phases

820   during metamorphic reactions. *Geological Materials Research*, 1, 1–49.

821 Rapp, R. P., Ryerson, F., & Miller, C. F. (1987). Experimental evidence bearing on the stability of

822   monazite during crustal anaatexis. *Geophysical Research Letters*, 14, 307–310.

823 Rapp, R. P., & Watson, E. B. (1986). Monazite solubility and dissolution kinetics: implications for the

824   thorium and light rare earth chemistry of felsic magmas. *Contributions to Mineralogy and*

825   *Petrology*, 94, 304–316.

826 Rosenberg, C. L., & Handy, M. R. (2005). Experimental deformation of partially melted granite

827   revisited: implications for the continental crust. *Journal of Metamorphic Geology*, 23, 19–28.

828   Rubatto, D. (2002). Zircon trace element geochemistry: partitioning with garnet and the link between U–

829   Pb ages and metamorphism. *Chemical Geology*, 184, 123–138.

830   Rubatto, D. (2017). Zircon: The Metamorphic Mineral. *Reviews in Mineralogy and Geochemistry*, 83,

831   261–295.

832   Rubatto, D., & Gebauer, D. (2000). Use of Cathodoluminescence for U-Pb Zircon Dating by Ion

833   Microprobe: Some Examples from the Western Alps. In: *Cathodoluminescence in Geosciences*

834   (eds Pagel, M., Barbin, V., Blanc, P. & Ohnenstetter, D.), pp. 373–400, Springer Berlin

835   Heidelberg, Berlin, Heidelberg.

836   Rubatto, D., & Hermann, J. (2007). Experimental zircon/melt and zircon/garnet trace element

837   partitioning and implications for the geochronology of crustal rocks. *Chemical Geology*, 241,

838   38–61.

839   Rubatto, D., Williams, I. S., & Buick, I. S. (2001). Zircon and monazite response to prograde

840   metamorphism in the Reynolds Range, central Australia. *Contributions to Mineralogy and*

841   *Petrology*, 140, 458–468.

842   Rudnick, R. L., & Gao, S. (2014). 4.1 - Composition of the Continental Crust A2 - Holland, Heinrich D.

843   In: *Treatise on Geochemistry (Second Edition)* (ed Turekian, K. K.), pp. 1–51, Elsevier, Oxford.

844   Sawka, W. N., & Chappell, B. W. (1986). The distribution of radioactive heat production in I‐ and S‐

845   type granites and residual source regions: Implications to high heat flow areas in the Lachlan

846   Fold Belt, Australia. *Australian Journal of Earth Sciences*, 33, 107–118.

847   Sawyer, E. W. (1987). The Role of Partial Melting and Fractional Crystallization in Determining

848   Discordant Migmatite Leucosome Compositions. *Journal of Petrology*, 28, 445–473.

849   Schaltegger, U., & Davies, J. H. F. L. (2017). Petrochronology of Zircon and Baddeleyite in Igneous

850   Rocks: Reconstructing Magmatic Processes at High Temporal Resolution. *Reviews in*

851   *Mineralogy and Geochemistry*, 83, 297–328.

852   Schaltegger, U., Fanning, C.M., Günther, D., Maurin, J.C., Schulmann, K., & Gebauer, D. (1999).

853   Growth, annealing and recrystallization of zircon and preservation of monazite in high-grade

854   metamorphism: conventional and in-situ U-Pb isotope, cathodoluminescence and microchemical

855   evidence. *Contributions to Mineralogy and Petrology*, 134, 186–201.

856   Skora, S., & Blundy, J. (2010). High-pressure Hydrous Phase Relations of Radiolarian Clay and

857   Implications for the Involvement of Subducted Sediment in Arc Magmatism. *Journal of*

858   *Petrology*, 51, 2211–2243.

859   Skora, S., & Blundy, J. (2012). Monazite solubility in hydrous silicic melts at high pressure conditions

860   relevant to subduction zone metamorphism. *Earth and Planetary Science Letters*, 321, 104–114.

861   Shaw, D. M. (1970). Trace element fractionation during anatexis. *Geochimica et Cosmochimica Acta*,

862   34, 237–243.

863   Solar, G. S., & Brown, M. (2001). Petrogenesis of Migmatites in Maine, USA: Possible Source of

864   Peraluminous Leucogranite in Plutons? *Journal of Petrology*, 42, 789–823.

865   Smithies, R. H., Howard, H. M., Evins, P. M., Kirkland, C. L., Kelsey, D. E., Hand, M., ... Belousova,

866   E. (2011). High-Temperature Granite Magmatism, Crust–Mantle Interaction and the

867   Mesoproterozoic Intracontinental Evolution of the Musgrave Province, Central Australia.

868   *Journal of Petrology*, 52, 931–958.

869   Spandler, C., Hermann, J., Arculus, R. & Mavrogenes, J. (2003). Redistribution of trace elements during

870   prograde metamorphism from lawsonite blueschist to eclogite facies; implications for deep

871   subduction-zone processes. *Contributions to Mineralogy and Petrology*, 146, 205–222.

872   Spear, F. S. (2010). Monazite–allanite phase relations in metapelites. *Chemical Geology*, 279, 55–62.

873   Spear, F. S., & Pyle, J. M. (2002). Apatite, monazite, and xenotime in metamorphic rocks. *Reviews in*

874   *Mineralogy and Geochemistry*, 48, 293–335.

875   Spear, F. S., & Pyle, J. M. (2010). Theoretical modeling of monazite growth in a low-Ca metapelite.

876   *Chemical Geology*, 273, 111–119.

877   Stepanov, A. S., Hermann, J., Rubatto, D., & Rapp, R. P. (2012). Experimental study of monazite/melt

878   partitioning with implications for the REE, Th and U geochemistry of crustal rocks. *Chemical*

879   *Geology*, 300, 200–220.

880   Sun, S. S. & Hanson, G. N. (1975). Origin of Ross Island basanitoids and limitations upon the

881   heterogeneity of mantle sources for alkali basalts and nephelinites. *Contributions to Mineralogy*

882   *and Petrology*, 52, 77–106.

883   Tartèse, R., & Boulvais, P. (2010). Differentiation of peraluminous leucogranites "en route" to the

884   surface. *Lithos*, 114, 353–368.

885   Taylor, R. J. M., Kirkland, C. L., & Clark, C. (2016). Accessories after the facts: Constraining the

886   timing, duration and conditions of high-temperature metamorphic processes. *Lithos*, 264, 239–

887   257.

888   Taylor, S. R., & McLennan, S. M. (1985). *The Continental Crust: Its composition and evolution*.

889   Oxford: Blackwell Scientific. 312 pp.

890   Tomkins, H. S., Powell, R., & Ellis, D. J. (2007). The pressure dependence of the zirconium in rutile

891   thermometer. *Journal of metamorphic Geology*, *25*, 703–713.

892   Van Westrenen, W., Blundy, J. & Wood, B. (1999). Crystal-chemical controls on trace element

893   partitioning between garnet and anhydrous silicate melt. *American Mineralogist*, 84, 838–847.

894   Vavra, G., Schmid, R., & Gebauer, D. (1999). Internal morphology, habit and U-Th-Pb microanalysis of

895   amphibolite-to-granulite facies zircons: geochronology of the Ivrea Zone (Southern Alps).

896   *Contributions to Mineralogy and Petrology*, 134, 380–404.

897   Villaros, A., Stevens, G., Moyen, J.-F., & Buick, I. S. (2009). The trace element compositions of S-type

898   granites: evidence for disequilibrium melting and accessory phase entrainment in the source.

899   *Contributions to Mineralogy and Petrology*, 158, 543–561.

900   Villaseca, C., Martín Romera, C., De la Rosa, J., & Barbero, L. (2003). Residence and redistribution of

901   REE, Y, Zr, Th and U during granulite-facies metamorphism: behaviour of accessory and major

902   phases in peraluminous granulites of central Spain. *Chemical Geology*, 200, 293–323.

903   Wark, D. A., & Miller, C. F. (1993). Accessory mineral behavior during differentiation of a granite

904   suite: monazite, xenotime and zircon in the Sweetwater Wash pluton, southeastern California,

905   U.S.A. *Chemical Geology*, 110, 49–67.

906   Watson, E. B. (1996). Dissolution, growth and survival of zircons during crustal fusion: kinetic

907   principals, geological models and implications for isotopic inheritance. *Earth and Environmental*

908   *Science Transactions of the Royal Society of Edinburgh*, 87, 43-56.

909   Weber, C., Barbey, P., Cuney, M., & Martin, H. (1985). Trace element behaviour during migmatization.

910   Evidence for a complex melt-residuum-fluid interaction in the St. Malo migmatitic dome

911   (France). *Contributions to Mineralogy and Petrology*, 90, 52–62.

912   Webster, J. D., & Piccoli, P. M. (2015). Magmatic apatite: a powerful, yet deceptive, mineral. *Elements*,

913   11, 177–182.

914   White, R. W., & Powell, R. (2002). Melt loss and the preservation of granulite facies mineral

915   assemblages. *Journal of Metamorphic Geology*, 20, 621–632.

916   White, R. W., Powell, R., & Holland, T. J. B. (2007). Progress relating to calculation of partial melting

917   equilibria for metapelites. *Journal of Metamorphic Geology*, 25, 511–527.

918   White, R.W., Powell, R., Holland, T.J.B., Johnson, T. E., & Green, E.C.R. (2014). New mineral

919   activity–composition relations for thermodynamic calculations in metapelitic systems. *Journal of*

920   *Metamorphic Geology*, 32, 261–286.

921   Williams, I. S., & Claesson, S. (1987). Isotopic evidence for the Precambrian provenance and

922   Caledonian metamorphism of high grade paragneisses from the Seve Nappes, Scandinavian

923   Caledonides. *Contributions to Mineralogy and Petrology*, 97, 205–217.

924   Williams, M. L., Jercinovic, M. J., & Hetherington, C. J. (2007). Microprobe Monazite Geochronology:

925   Understanding Geologic Processes by Integrating Composition and Chronology. *Annual Review*

926   *of Earth and Planetary Sciences*, 35, 137–175.

927   Wing, B. A., Ferry, J. M., & Harrison, T. M. (2003). Prograde destruction and formation of monazite

928   and allanite during contact and regional metamorphism of pelites: petrology and geochronology.

929   *Contributions to Mineralogy and Petrology*, 145, 228–250.

930   Wolf, M. B., & London, D. (1994). Apatite dissolution into peraluminous haplogranitic melts: an

931   experimental study of solubilities and mechanisms. *Geochimica et Cosmochimica Acta*, 58,

932   4127–4145.

933   Xing, L., Trail, D., & Watson, E. B. (2013). Th and U partitioning between monazite and felsic melt.

934   *Chemical Geology*, 358, 46–53.

935   Yakymchuk, C. (2017). Behaviour of apatite during partial melting of metapelites and consequences for

936   prograde suprasolidus monazite growth. *Lithos*, 274–275, 412–426.

937   Yakymchuk, C., & Brown, M. (2014a). Consequences of open-system melting in tectonics. *Journal of*

938   *the Geological Society*, 171, 21–40.

939   Yakymchuk, C. & Brown, M., (2014b). Behaviour of zircon and monazite during crustal melting.

940   *Journal of the Geological Society*, 171, 465–479.

941   Yakymchuk, C., Clark, C., & White, R. W. (2017). Phase Relations, Reaction Sequences and

942   Petrochronology. *Reviews in Mineralogy and Geochemistry*, 83, 13–53.

943   Yang, P., & Rivers, T. (2004). The origin of Mn and Y annuli in garnet and the thermal dependence of P

944   in garnet and Y in apatite in calc-pelite and pelite, Gagnon terrane, western Labrador. *American*

945   *Mineralogist*, 88, 1398–1398.

946 **FIGURE CAPTIONS**

947

948 **FIGURE 1.** (a) Th/U ratios of metamorphic zircon from Western Australia. (b) Concentrations of Th in

949 metamorphic zircon from Western Australia. (c) Concentration of U in metamorphic zircon from

950 Western Australia. (d) Th/U ratios of igneous zircon from Western Australia. (e) Concentrations of Th

951 in igneous zircon from Western Australia. (f) Concentration of U in igneous zircon from Western

952 Australia. The inset in each panel is the log-normalized data.

953

954 **FIGURE 2.** Concentration of Th in monazite and melt in experimental glasses and from granites and

955 leucosomes in natural samples. Experimental results from Stepanov et al. (2012) and Xing et al. (2013).

956 Glass compositions from Hermann and Rubatto (2009) are paired with the monazite compositions

957 reported in Skora and Blundy (2010). The Macusani glass composition (JV2 from Pichavant et al., 1987)

958 is paired with the average concentration of Th in monazite from Montel (1993). Nanogranite and paired

959 monazite compositions are from Acosta-Vigil et al. (2010). Monazite and co-existing granite/leucosome

960 are from Förster (1998), Bea et al. (1994), Wark and Miller (1983) Weber et al. (1995) and Breiter

961 (2016). The range of leucosome and peraluminous granite Th concentrations are from Inger and Harris

962 (1993), Villaros et al. (2009), Tartèse and Boulvais (2010), Sawyer (1987), Solar and Brown (2001), and

963 Korhonen et al. (2010).

964

965 **FIGURE 3**. *P–T* phase diagram for an average amphibolite-facies metapelite composition from Ague

966 (1991). The dashed line is the solidus. Mineral abbreviations are from Holland and Powell (2011).

967

968 **FIGURE 4**. (a) Percentage of melt present over the modelled *P–T* range in mol.% (approximately

969 equivalent to vol.%). (b) Percentage of zircon dissolution relative to the amount at the solidus. (c)

41

970 Percentage of monazite dissolution relative to the amount at the solidus. (d) Percentage of apatite

971 dissolution relative to the amount at the solidus. The dashed line is the solidus.

972

973 **FIGURE 5.** Th and U concentrations and Th/U ratio of anatectic melt and zircon. Dashed lines are these

974 values outside the stability of zircon in the modelled composition. The thick black lines are the wet

975 solidus in each panel. Abbreviations are apatite (ap), zircon (zrc), and monazite (mnz).

976

977 **FIGURE 6.** Contours of Th/U = 0.1 of zircon for various parameters in the modelling. (a)

978 $D^{Th}_{mnz/melt}$ values ranging from 3,000 to 100,000. Note that values <3,000 do not allow zircon with

979 Th/U<0.1 over the modelled *P–T* conditions for this bulk composition. (b) Bulk rock LREE

980 concentrations ranging from 50–500 ppm, which represents an approximation for the amount of

981 monazite in the system. (c) Bulk rock U concentrations ranging from 2 to 18 ppm for a constant Th

982 concentration of 14 ppm. (d) Bulk rock Th concentrations ranging from 4 to 20 ppm for a constant U

983 concentration of 3.5 ppm.

984

985 **FIGURE 7**. Closed-system isobaric heating path at 0.6 GPa. (a) Normalized molar proportions of major

986 phases. Melt production is non-linear and has two 'pulses' of melting at muscovite breakdown at

987 ~700°C and biotite breakdown at ~810°C. (b) Concentrations of Th and U in the melt and residue

988 calculated by mass balance. (c) Percentage of monazite, apatite and zircon remaining during heating.

989 Note that dissolution of all accessory minerals is not linear and is at a faster rate during muscovite and

990 biotite breakdown at ~700°C and ~810°C respectively. (d) Thorium budget of the system. (e) Uranium

991 budget of the system. Monazite and zircon each contain roughly 20–30 wt.% of the U in the system at

992 the solidus. (f) Approximate concentration of ThO$_2$ (wt.%) in monazite. Thorium content in monazite

993 increases during heating. (g) Concentration of U in zircon in equilibrium with anatectic melt decreases

994 with temperature. (h) Concentration of Th in zircon in equilibrium with melt initially decreases up

42

995   temperature and then increases, which reflects the breakdown of monazite. After monazite is depleted at

996   ~845°C, the concentration is no longer buffered by monazite and the concentration of Th in zircon

997   decreases. (i) Th/U ratio of zircon increases during heating and rises above 0.1 at ~800°C. The Th/U

998   ratio of zircon increases until monazite is consumed and then steadily decreases at > 845°C.

999

1000   **FIGURE 8.** Closed-system isobaric heating path at 0.9 GPa. (a) Normalized molar proportions of major

1001   phases. (b) Concentrations of Th and U in the melt and residue calculated by mass balance. (c)

1002   Percentage of monazite, apatite and zircon remaining during heating. (d) Thorium budget of the system.

1003   (e) Uranium budget of the system. (f) Approximate concentration of ThO_2 (wt.%) in monazite. Thorium

1004   content in monazite increases during heating. (g) Concentration of U in zircon in equilibrium with

1005   anatectic melt decreases with temperature. (h) Concentration of Th in zircon in equilibrium with melt

1006   initially decreases up temperature and then increases, which reflects the breakdown of monazite. After

1007   monazite is depleted at ~840°C, the concentration is no longer buffered by monazite and the

1008   concentration of Th in zircon decreases. (i) Th/U ratio of zircon increases during heating and rises above

1009   0.1 at ~770°C. The Th/U ratio of zircon increases until monazite is consumed and then steadily

1010   decreases at > 840°C.

1011

1012   **FIGURE 9.** Open-system isobaric heating path at 0.9 GPa. (a) Normalized molar proportions of major

1013   phases. (b) Proportion of accessory minerals remaining relative to the amount at the wet solidus. (c)

1014   Concentrations of U (ppm) in the melt, residue and the system calculated by mass balance. (d)

1015   Concentrations of Th (ppm) in the melt, residue and the system. (e) Concentrations of P_2O_5 (wt.%) in the

1016   melt, residue and the system. (f) Concentration of ThO_2 in monazite. (g) Concentration of U in zircon.

1017   (f) Concentration of Th in zircon. (g) Th/U ratio of zircon. The bold dashed line is the wet solidus. ML:

1018   melt loss event.

1019

43

1020   **FIGURE 10.** Sensitivity of Th/U ratio of zircon in equilibrium with melt to various model parameters

1021   for an isobaric heating path at 0.9 GPa in an open system. $LREE_{WR}$: concentration of LREE in the

1022   system. U_{WR}: concentration of Uranium in the system. ML: melt loss event. S: solidus for melt loss

1023   event number (i.e. S5 is the solidus after ML5).

1024

1025   **FIGURE 11.** Time required for dissolution of accessory minerals of various diameters and

1026   concentrations of H_2O in melt. (a) Zircon (modified from Harrison & Watson, 1983). (b) Monazite

1027   (modified from Rapp & Watson, 1986). (c) Apatite (modified from Harrison & Watson, 1984).

1028

1029   **SUPPLEMENTARY TABLE S1.** Th and U concentration in metamorphic zircon grains.

Table 1. Bulk composition used in phase equilibria modelling (mol.%)

Figures		H_2O	SiO_2	Al_2O_3	CaO	MgO	FeO	K_2O	Na_2O	TiO_2	MnO	O
Closed system												
7	0.6 GPa	5.15	61.23	12.94	1.50	5.24	7.61	2.79	1.90	0.86	0.17	0.61
3–8	0.9 GPa	6.24	60.55	12.80	1.49	5.18	7.52	2.76	1.88	0.85	0.16	0.60
Open system												
9	0.9 GPa, ML1	4.93	60.67	13.13	1.55	5.50	7.98	2.76	1.77	0.90	0.17	0.64
9	0.9 GPa, ML2	3.56	60.80	13.48	1.61	5.84	8.47	2.75	1.67	0.96	0.19	0.68
9	0.9 GPa, ML3	2.32	60.78	13.83	1.67	6.20	8.98	2.73	1.56	1.02	0.20	0.72
9	0.9 GPa, ML4	1.17	60.64	14.17	1.72	6.57	9.52	2.70	1.46	1.08	0.21	0.77
9	0.9 GPa, ML5	0.18	60.33	14.50	1.76	6.96	10.08	2.64	1.37	1.15	0.22	0.82

ML: melt loss event

Table 2. Partition coefficients used in modelling (mineral/melt)

Mineral	Abbreviation	D_U	D_{Th}	Source	Experimental run
Biotite	bi	0.17	1.227	Mahood and Hildreth (1983)	Average
Cordierite	cd	1.61	0.1	Bea et al. (1994)	Average
Garnet	g	0.227	0.1188	van Westrenen et al. (1999)	Average
K-Feldspar	ksp	0.048	0.023	Nash and Crecraft (1985)	Average
Plagioclase	pl	0.093	0.048	Nash and Crecraft (1985)	Average
Quartz	q	0.025	0.08	Nash and Crecraft (1985)	Average
Muscovite	mu	n.d.	n.d.	–	–
Ilmenite	ilm	0.01	0.0027	Klemme et al. (2006)	HD10-1
Rutile	ru	3.8	0.00014	Klemme et al. (2005)	MHD16_1 D
Apatite	ap	0.476	0.733	Prowatke and Klemme (2006)	Average
Zircon	zrc	various	various	Kirkland et al. (2015)	equations (1), (2)
Monazite	mnz	83	various	Stepanov et al. (2012), see text	Average, see text

n.d. = no data
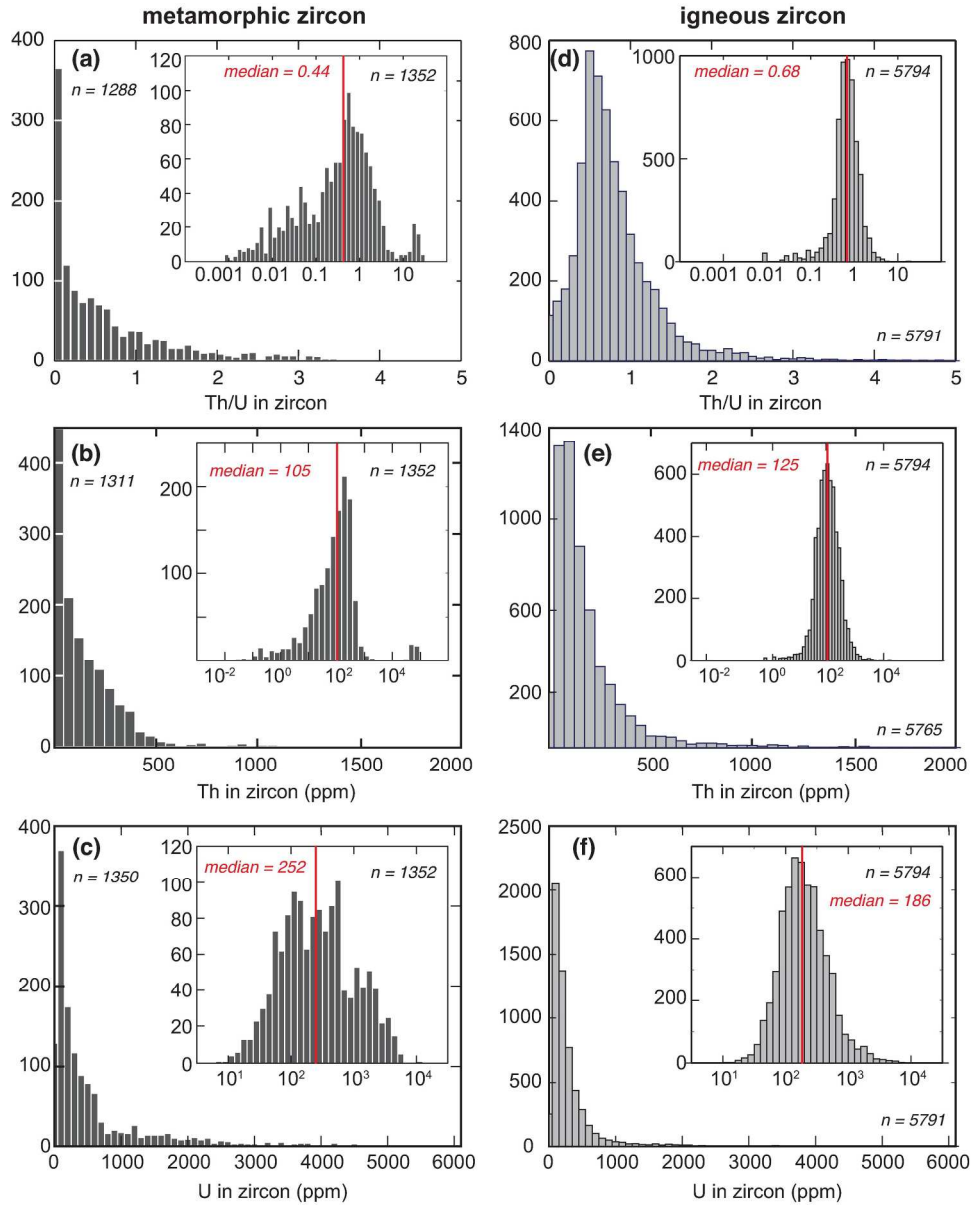
1

FIGURE 1. (a) Th/U ratios of metamorphic zircon from Western Australia. (b) Concentrations of Th in metamorphic zircon from Western Australia. (c) Concentration of U in metamorphic zircon from Western Australia. (d) Th/U ratios of igneous zircon from Western Australia. (e) Concentrations of Th in igneous zircon from Western Australia. (f) Concentration of U in igneous zircon from Western Australia. The inset in each panel is the log-normalized data.
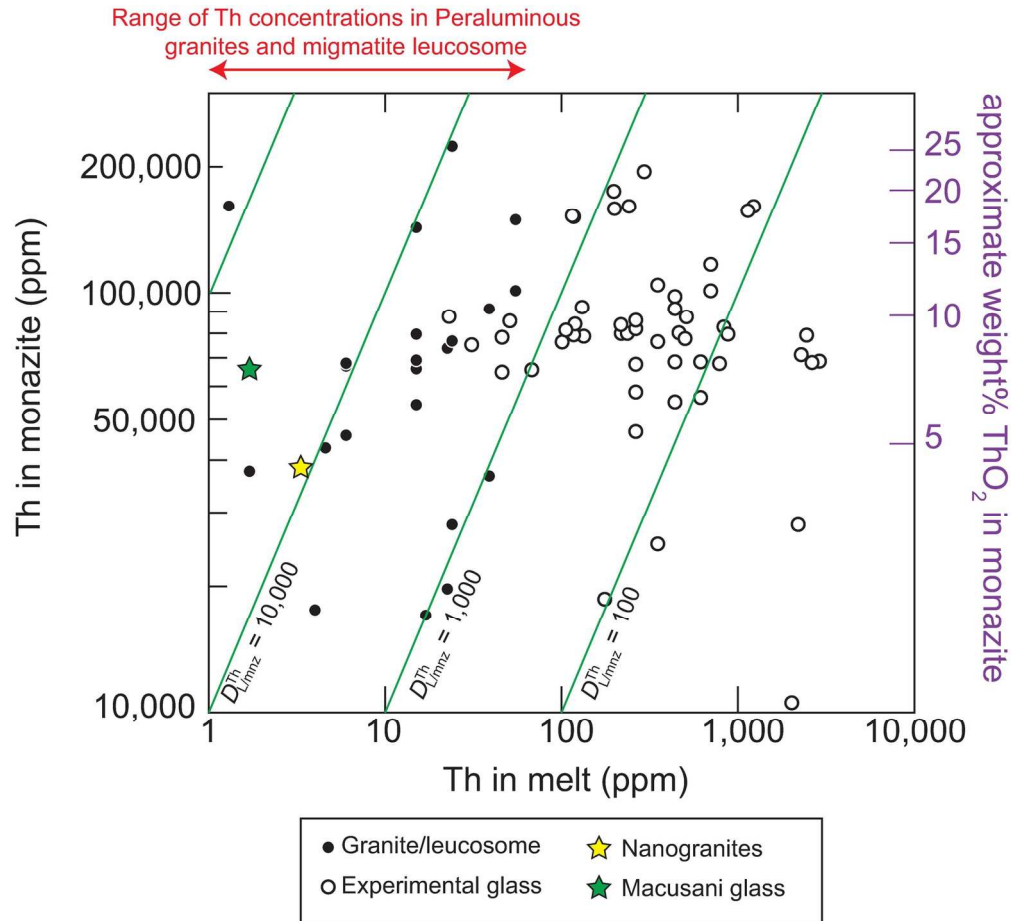
215x269mm (300 x 300 DPI)

FIGURE 2. Concentration of Th in monazite and melt in experimental glasses and from granites and leucosomes in natural samples. Experimental results from Stepanov et al. (2012) and Xing et al. (2013). Glass compositions from Hermann and Rubatto (2009) are paired with the monazite compositions reported in Skora and Blundy (2010). The Macusani glass composition (JV2 from Pichavant et al., 1987) is paired with the average concentration of Th in monazite from Montel (1993). Nanogranite and paired monazite compositions are from Acosta-Vigil et al. (2010). Monazite and co-existing granite/leucosome are from Förster (1998), Bea et al. (1994), Wark and Miller (1983) Weber et al. (1995) and Breiter (2016). The range of leucosome and peraluminous granite Th concentrations are from Inger and Harris (1993), Villaros et al. (2009), Tartèse and Boulvais (2010), Sawyer (1987), Solar and Brown (2001), and Korhonen et al. (2010).

159x145mm (300 x 300 DPI)
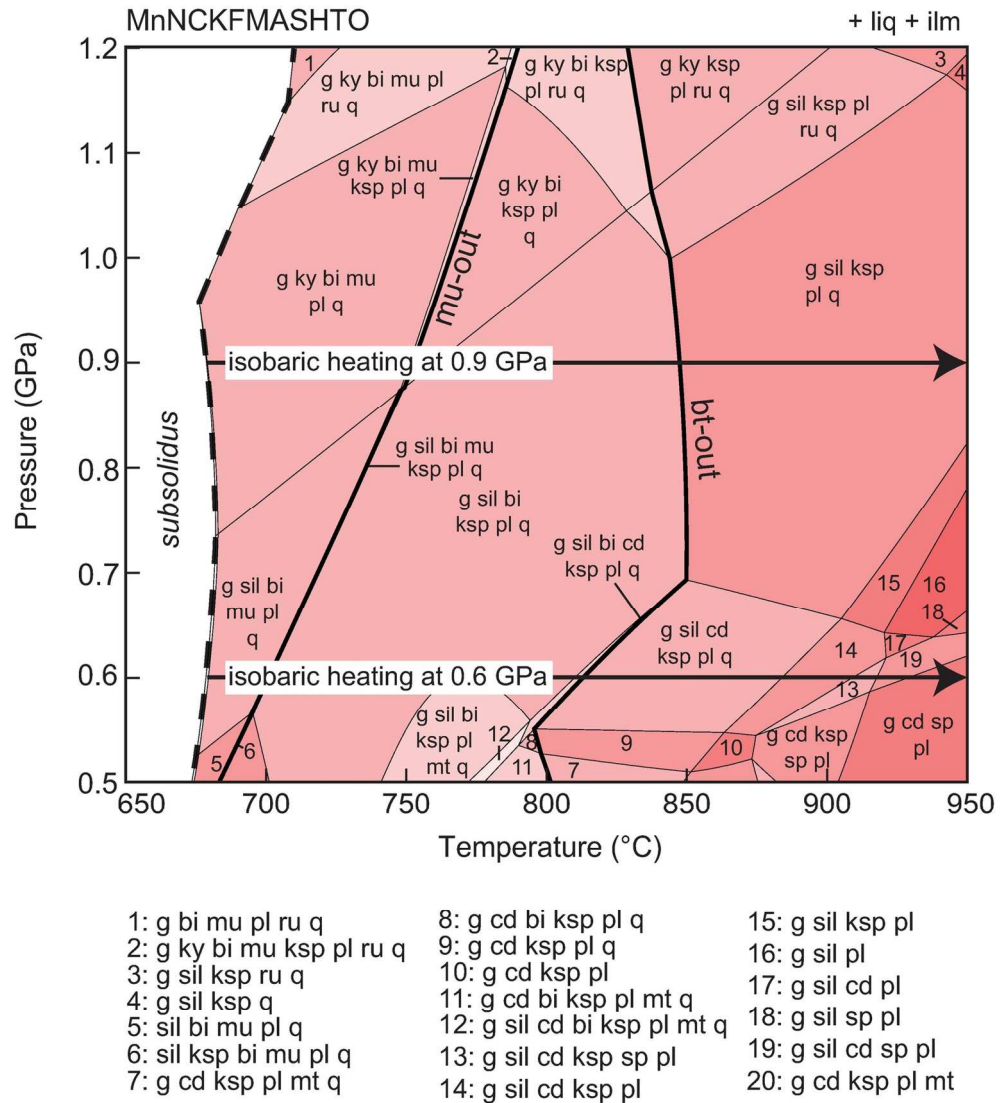
FIGURE 3. P–T phase diagram for an average amphibolite-facies metapelite composition from Ague (1991). The dashed line is the solidus. Mineral abbreviations are from Holland and Powell (2011).

147x162mm (300 x 300 DPI)
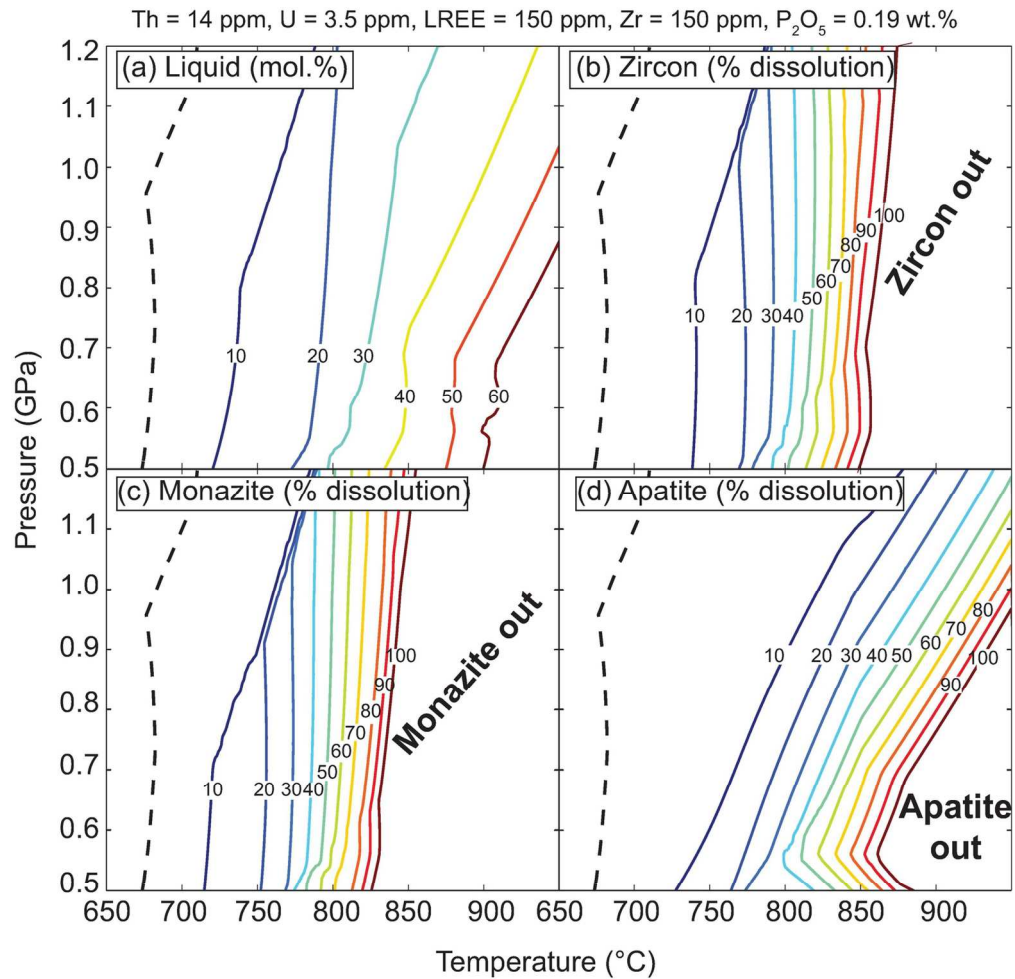
FIGURE 4. (a) Percentage of melt present over the modelled P–T range in mol.% (approximately equivalent to vol.%). (b) Percentage of zircon dissolution relative to the amount at the solidus. (c) Percentage of monazite dissolution relative to the amount at the solidus. (d) Percentage of apatite dissolution relative to the amount at the solidus. The dashed line is the solidus.

143x139mm (300 x 300 DPI)
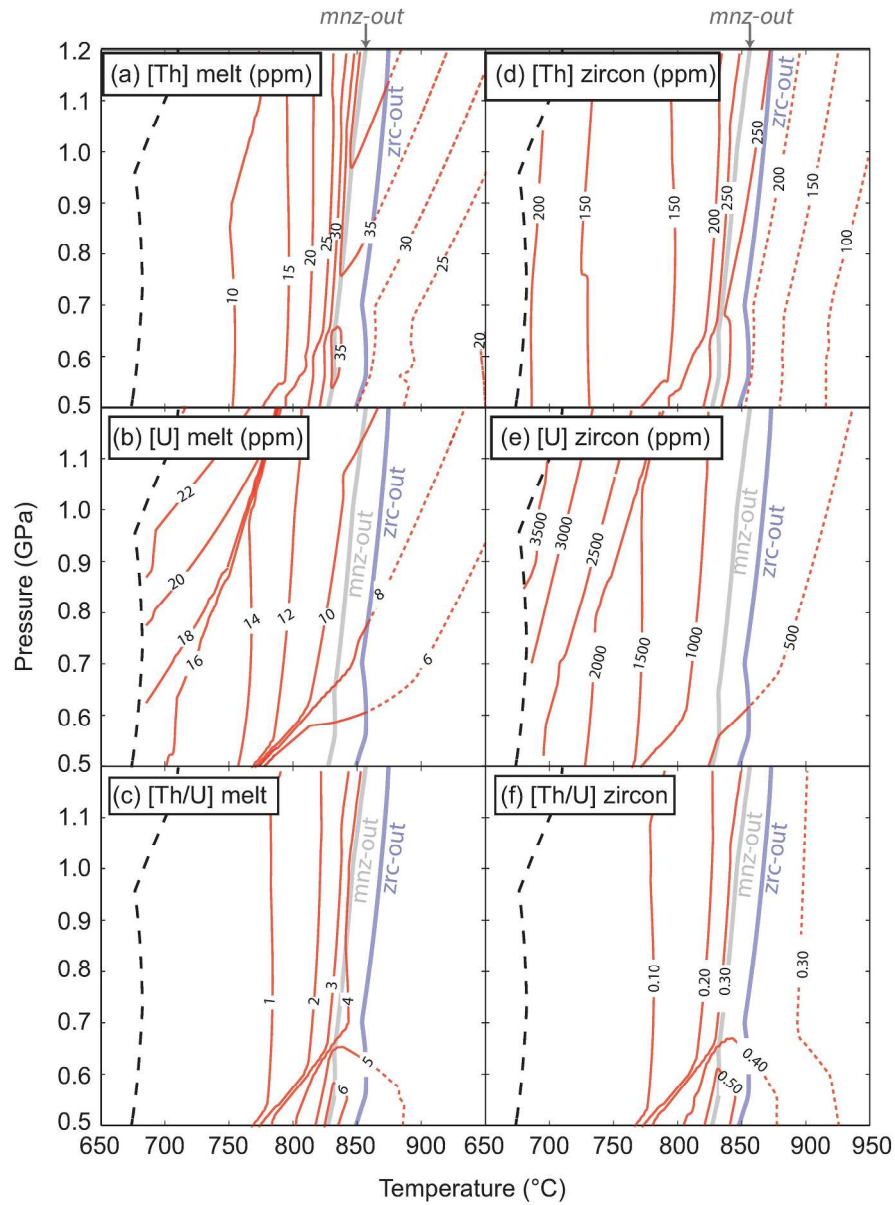
FIGURE 5. Th and U concentrations and Th/U ratio of anatectic melt and zircon. Dashed lines are these values outside the stability of zircon in the modelled composition. The thick black lines are the wet solidus in each panel. Abbreviations are apatite (ap), zircon (zrc), and monazite (mnz).

208x283mm (300 x 300 DPI)
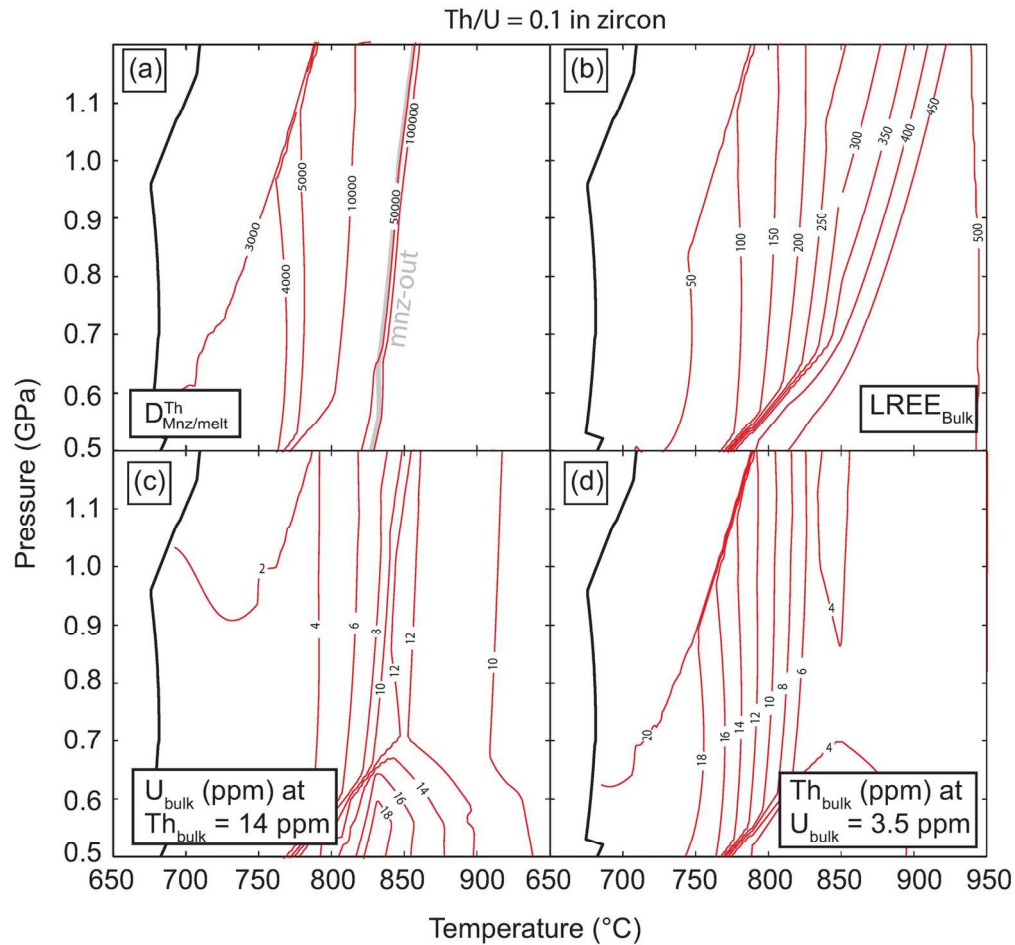
FIGURE 6. Contours of Th/U = 0.1 of zircon for various parameters in the modelling. (a) $D_{mnz/melt}^{Th}$ values ranging from 3,000 to 100,000. Note that values <3,000 do not allow zircon with Th/U<0.1 over the modelled P–T conditions for this bulk composition. (b) Bulk rock LREE concentrations ranging from 50–500 ppm, which represents an approximation for the amount of monazite in the system. (c) Bulk rock U concentrations ranging from 2 to 18 ppm for a constant Th concentration of 14 ppm. (d) Bulk rock Th concentrations ranging from 4 to 20 ppm for a constant U concentration of 3.5 ppm.

144x135mm (300 x 300 DPI)
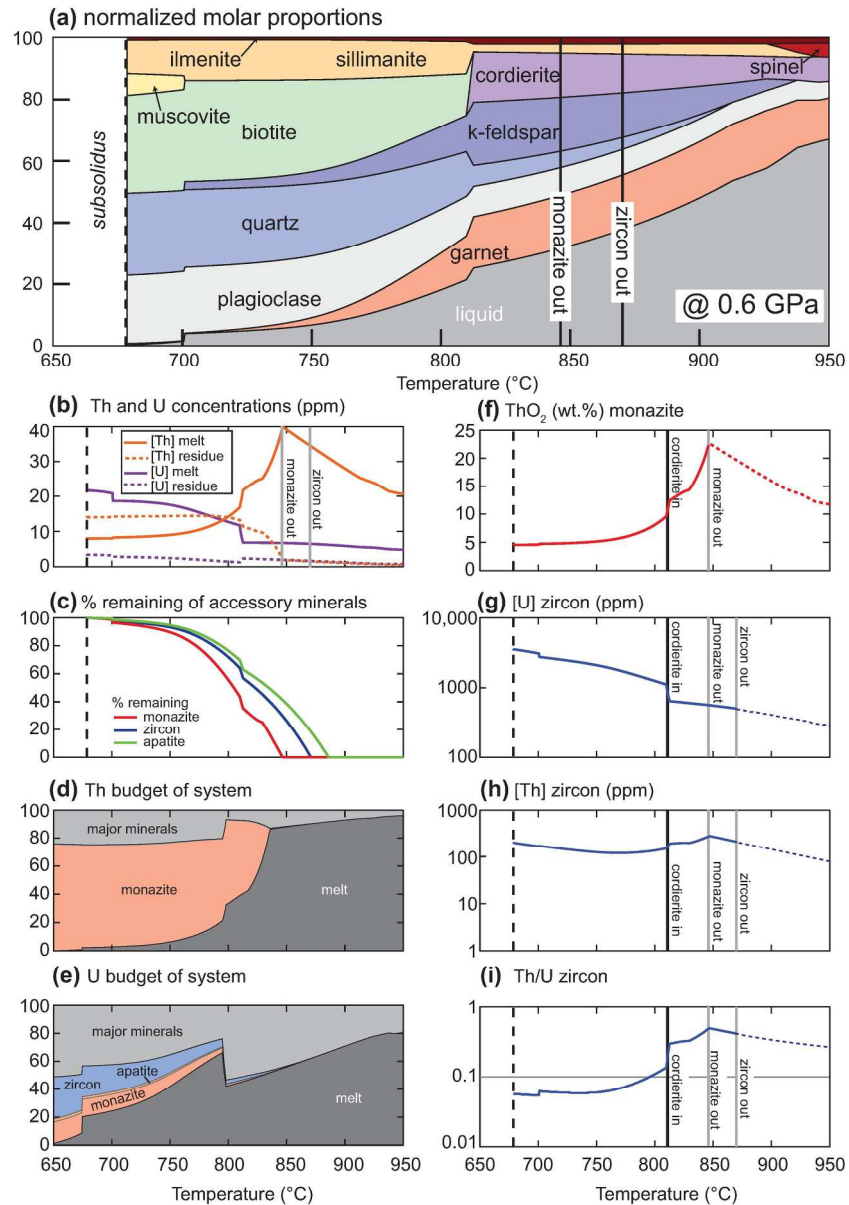
FIGURE 7. Closed-system isobaric heating path at 0.6 GPa. (a) Normalized molar proportions of major phases. Melt production is non-linear and has two 'pulses' of melting at muscovite breakdown at ~700°C and biotite breakdown at ~810°C. (b) Concentrations of Th and U in the melt and residue calculated by mass balance. (c) Percentage of monazite, apatite and zircon remaining during heating. Note that dissolution of all accessory minerals is not linear and is at a faster rate during muscovite and biotite breakdown at ~700°C and ~810°C respectively. (d) Thorium budget of the system. (e) Uranium budget of the system. Monazite and zircon each contain roughly 20–30 wt.% of the U in the system at the solidus. (f) Approximate concentration of ThO2 (wt.%) in monazite. Thorium content in monazite increases during heating. (g) Concentration of U in zircon in equilibrium with anatectic melt decreases with temperature. (h) Concentration of Th in zircon in equilibrium with melt initially decreases up temperature and then increases, which reflects the breakdown of monazite. After monazite is depleted at ~845°C, the concentration is no longer buffered by monazite and the concentration of Th in zircon decreases. (i) Th/U ratio of zircon increases during heating and rises above 0.1 at ~800°C. The Th/U ratio of zircon increases until monazite is
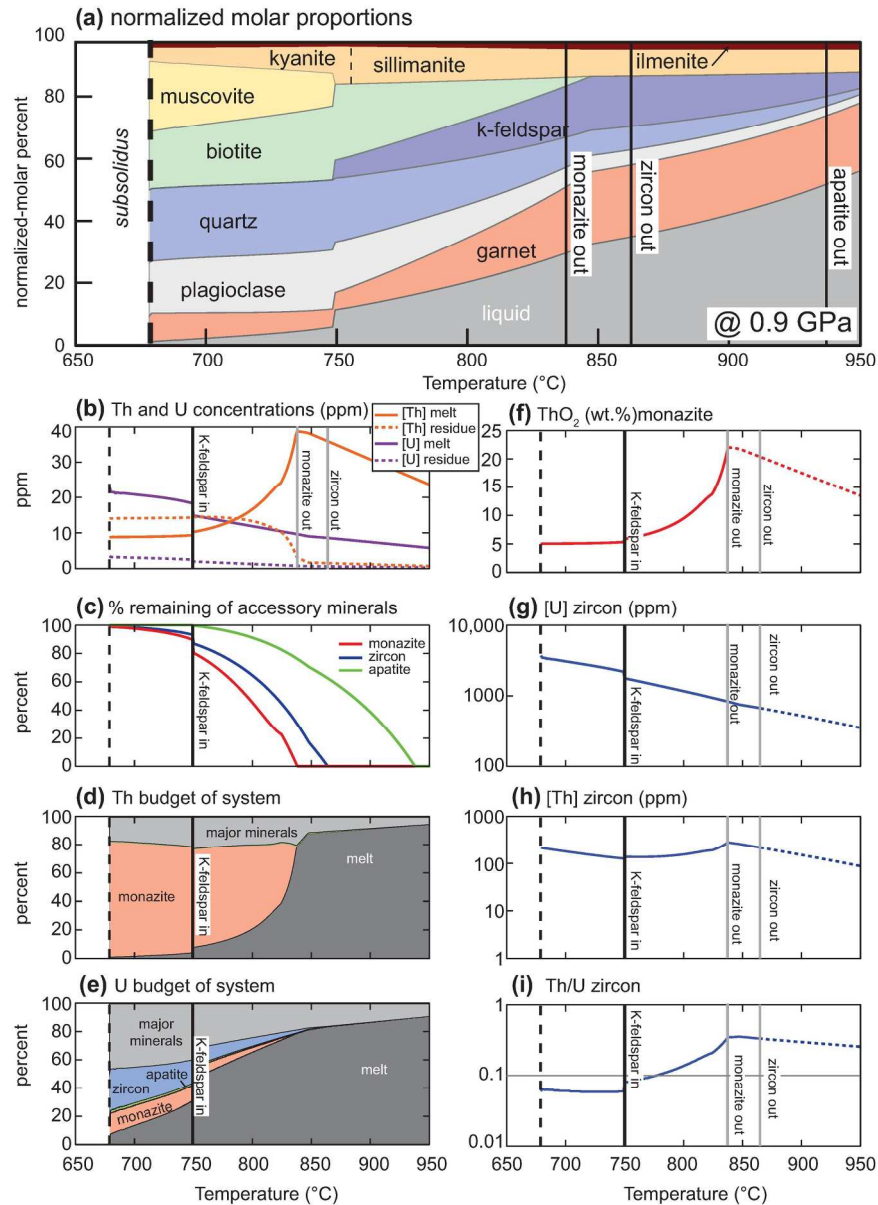
FIGURE 8. Closed-system isobaric heating path at 0.9 GPa. (a) Normalized molar proportions of major phases. (b) Concentrations of Th and U in the melt and residue calculated by mass balance. (c) Percentage of monazite, apatite and zircon remaining during heating. (d) Thorium budget of the system. (e) Uranium budget of the system. (f) Approximate concentration of ThO2 (wt.%) in monazite. Thorium content in monazite increases during heating. (g) Concentration of U in zircon in equilibrium with anatectic melt decreases with temperature. (h) Concentration of Th in zircon in equilibrium with melt initially decreases up temperature and then increases, which reflects the breakdown of monazite. After monazite is depleted at ~840°C, the concentration is no longer buffered by monazite and the concentration of Th in zircon decreases. (i) Th/U ratio of zircon increases during heating and rises above 0.1 at ~770°C. The Th/U ratio of zircon increases until monazite is consumed and then steadily decreases at > 840°C.
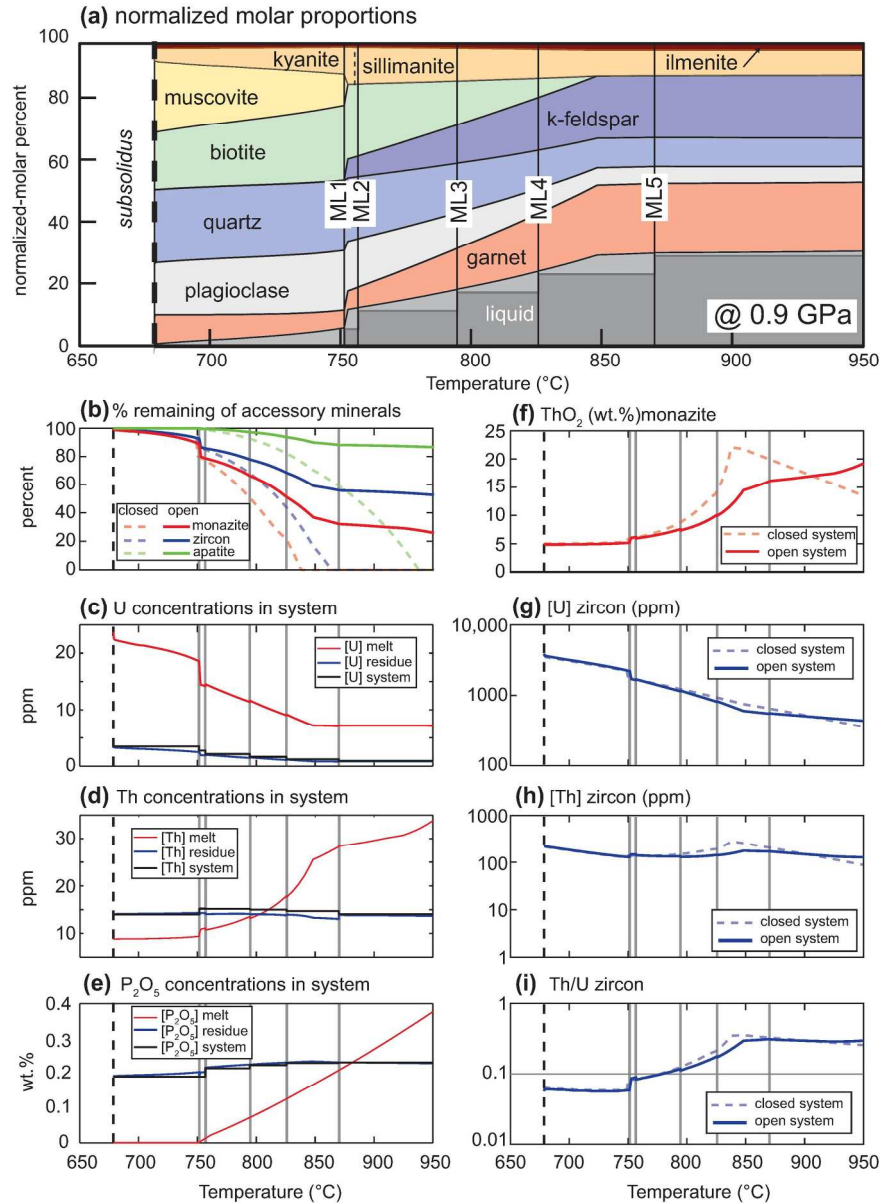
181x251mm (300 x 300 DPI)

FIGURE 9. Open-system isobaric heating path at 0.9 GPa. (a) Normalized molar proportions of major phases. (b) Proportion of accessory minerals remaining relative to the amount at the wet solidus. (c) Concentrations of U (ppm) in the melt, residue and the system calculated by mass balance. (d) Concentrations of Th (ppm) in the melt, residue and the system. (e) Concentrations of P2O5 (wt.%) in the melt, residue and the system. (f) Concentration of ThO2 in monazite. (g) Concentration of U in zircon. (f) Concentration of Th in zircon. (g) Th/U ratio of zircon. The bold dashed line is the wet solidus. ML: melt loss event.
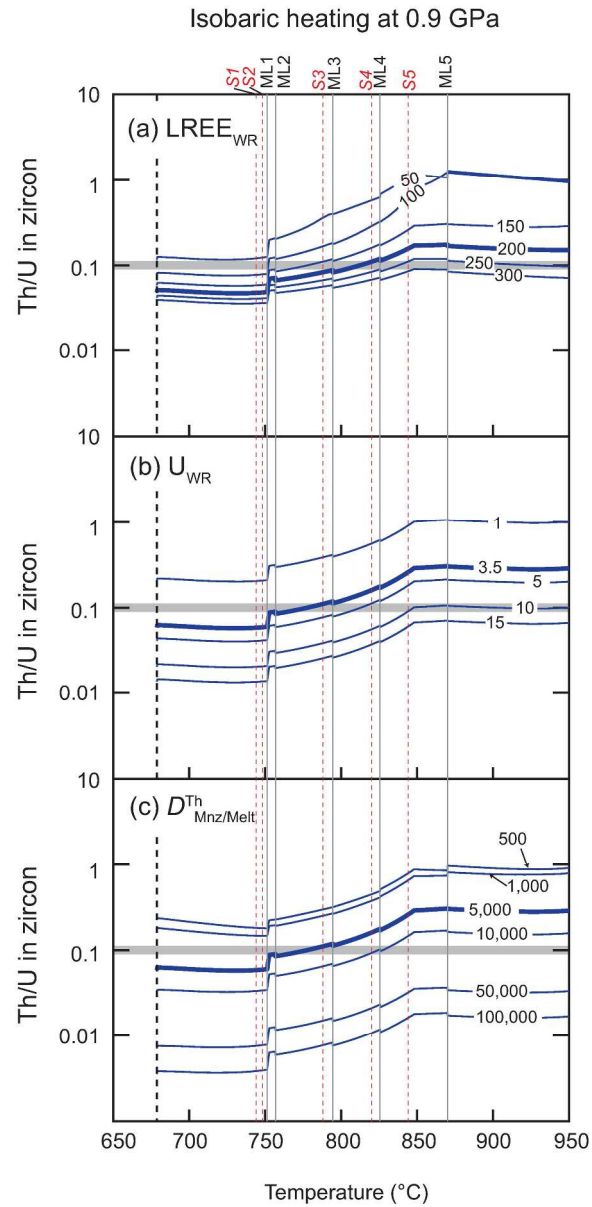
181x251mm (300 x 300 DPI)

FIGURE 10. Sensitivity of Th/U ratio of zircon in equilibrium with melt to various model parameters for an isobaric heating path at 0.9 GPa in an open system. LREEWR: concentration of LREE in the system. UWR: concentration of Uranium in the system. ML: melt loss event. S: solidus for melt loss event number (i.e. S5 is the solidus after ML5).
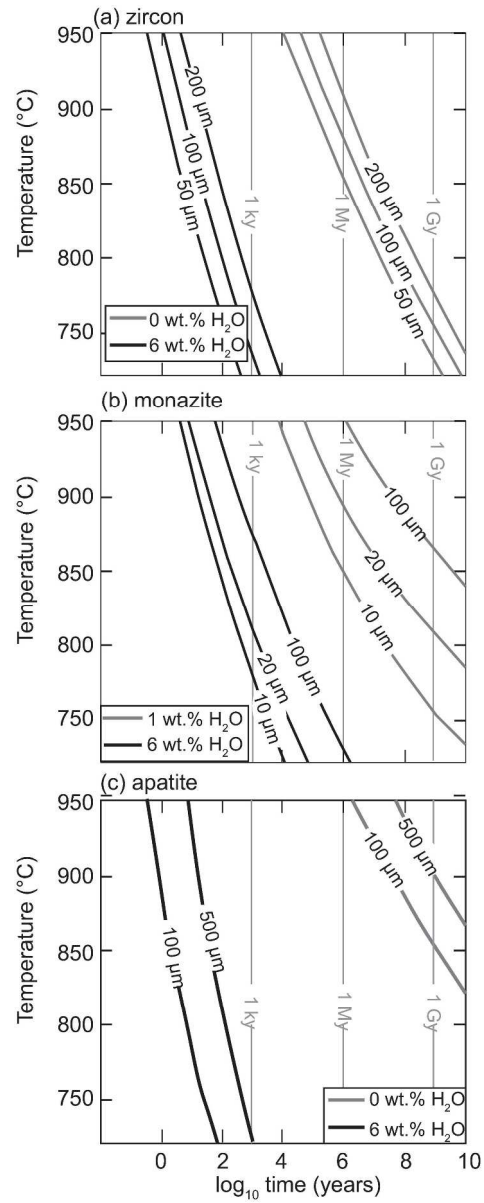
198x414mm (300 x 300 DPI)

FIGURE 11. Time required for dissolution of accessory minerals of various diameters and concentrations of H2O in melt. (a) Zircon (modified from Harrison & Watson, 1983). (b) Monazite (modified from Rapp & Watson, 1986). (c) Apatite (modified from Harrison & Watson, 1984).

196x505mm (300 x 300 DPI)